Atmos. Chem. Phys., 25, 7343–7368, 2025
https://doi.org/10.5194/acp-25-7343-2025

Atmospheric Chemistry and Physics
Open Access
EGU

Research article

Volcanic emission estimates from the inversion of ACTRIS lidar observations and their use for quantitative dispersion modeling

Anna Kampouri[1,2], Vassilis Amiridis[1], Thanasis Georgiou[1,3], Stavros Solomos[4], Anna Gialitaki[1,5], Maria Tsichla[1,6], Michael Rennie[7], Simona Scollo[8], and Prodromos Zanis[2]

[1]Institute for Astronomy, Astrophysics, Space Applications and Remote Sensing (IAASARS), National Observatory of Athens, 10560 Athens, Greece
[2]Department of Meteorology and Climatology, School of Geology, Aristotle University of Thessaloniki, 54124 Thessaloniki, Greece
[3]Laboratory of Atmospheric Physics, School of Physics, Aristotle University of Thessaloniki, 54124 Thessaloniki, Greece
[4]Research Centre for Atmospheric Physics and Climatology, Academy of Athens, 10680 Athens, Greece
[5]Department of Physics and Astronomy, Earth Observation Science Group, University of Leicester, Leicester LE1 7RH, UK
[6]Environmental Chemical Processes Laboratory, Department of Chemistry, University of Crete, Heraklion, Greece
[7]European Centre for Medium-Range Weather Forecasts, Reading RG2 9AX, UK
[8]Istituto Nazionale di Geofisica e Vulcanologia, Osservatorio Etneo, 95125 Catania, Italy

Correspondence: Anna Kampouri (akampouri@noa.gr)

Received: 14 October 2024 – Discussion started: 3 January 2025
Revised: 28 March 2025 – Accepted: 28 March 2025 – Published: 14 July 2025

Abstract. Modeling the dispersion of volcanic particles following explosive eruptions is critical for aviation safety. To constrain the dispersion of volcanic plumes and assess hazards, calculations rely on the accurate characterization of the eruption's source term, e.g., variation in emission rate and column height with time and the prevailing wind fields. This study introduces an inverse modeling framework that integrates a Lagrangian dispersion model with lidar observations to estimate emission rates of volcanic particles released during an Etna eruption. The methodology consists of using the FLEXPART model to generate source–receptor relationships (SRRs) between the volcano and the lidar system that observed the volcanic plume. These SRRs are then used to derive the emission rates based on observational data, including volcanic ash plume heights from the INGV-EO observatory and Polly^{XT} lidar retrievals. We leverage data from the ACTRIS Polly^{XT} lidar that operates at the PANhellenic GEophysical observatory of Antikythera of the National Observatory of Athens (PANGEA-NOA). The inversion algorithm utilizes lidar observations and an empirical a priori emission profile to estimate the volcanic particle source strength, accounting for altitude and time of the plume's evolution. Additionally, to study the impact that the wind fields have on volcanic ash forecasting, the experiment is repeated using fields that assimilate Aeolus wind lidar data. Our approach applied to the 12 March 2021 Etna eruption and accurately captures a dense aerosol layer between 8 and 12 km above the PANGEA-NOA station. Results show a minimal difference of the order of 2 % between the observed and the simulated ash concentrations. Furthermore, the structure of the a posteriori ash plume closely resembles the ash cloud image captured by the SEVIRI satellite above Antikythera island, highlighting the novelty of the inversion results. The presented inversion algorithm, coupled with Aeolus data, optimizes both the vertical emission distribution and Etna emission rates, advancing our understanding and preparedness for volcanic events.

Published by Copernicus Publications on behalf of the European Geosciences Union.

1 Introduction

Volcanic ash constitutes a significant hazard to aviation when it is emitted at aircraft cruising altitudes (9–11 km), with potential consequences including aircraft engine failure (Guffanti et al., 2005), inaccurate readings of critical navigational instruments, and reduced visibility due to external aircraft corrosion (Clarkson and Simpson, 2017; ICAO, 2016).

In the case of a volcanic eruption, urgent decisions are necessary to determine safe flight routes and to ensure that airborne aircraft land safely. While safety remains the top priority, the grounding and rerouting of flights lead to large financial losses, e.g., the 2010 eruption of Eyjafjallajökull in Iceland reportedly cost the airline industry over USD 1 billion (Mazzocchi et al., 2010; Oxford Economics, 2012).

Information on volcanic ash dispersion after an eruption is provided to operators by specialized early warning systems (EWSs) operated by the Volcanic Ash Advisory Centers (VAACs) (Fearnley et al., 2018). These systems typically rely on deterministic volcanic ash transport and dispersion models (VATDM) to offer short-term forecasts of the volcanic ash cloud. Although VAACs specify the expected location of the ash cloud, usually they do not provide quantitative information about ash concentration. In the spotlight of the expected rise in the number of flights over volcanically active regions in the near future (as indicated by EUROCONTROL, 2022), the probability of encountering volcanic ash at aircraft cruising altitudes will proportionally increase. Consequently, the challenge is to minimize uncertainties in short-term forecasts of volcanic ash dispersion.

The primary sources of uncertainties in deterministic transport models originate from the eruption source parameters, the various model parameterizations (such as wet deposition), and the driving meteorological conditions (Dacre et al., 2011; Prata and Lynch, 2019; Stohl et al., 2011). Typically, volcanic ash transport and dispersion models (VATDMs) require the specification of parameters about the volcanic event, including a vertical profile of ash emission rates, particle size distribution, and ash density (Harvey et al., 2020). The eruption start time can be estimated through satellite observations or by local volcano observatories. Various remote sensing techniques exist to estimate the height of the ash plume (Petersen et al., 2012). It should be mentioned that information that relies on observations from passive sensors has limited sensitivity to the ash layer height. Mass eruption rates are typically evaluated using empirical relationships based on observed plume heights (Mastin et al., 2009). However, these empirical relationships often fail to consider secondary factors influencing plume height, such as meteorological conditions. The long-range transport of volcanic particles is influenced by tropospheric and/or stratospheric winds, particularly the vertical wind shear, which is frequently inaccurately represented in numerous numerical weather prediction (NWP) models (Harvey et al., 2020; Houchi et al., 2010; Stoffelen et al., 2020).

Moreover, volcanic particles can influence the planetary radiative balance through both direct and indirect effects, introducing significant uncertainties in plume dispersion and lifetime. The direct effect involves the scattering and absorption of solar and terrestrial radiation, where fine ash and sulfate aerosols contribute to surface cooling or atmospheric warming depending on particle composition, size distribution, and injection plume height (Robock, 2000; Sicard et al., 2025). The indirect effect relates to the role of volcanic particles in cloud micro- and macrophysical properties. Ash particles can act as cloud condensation nuclei (CCN), facilitating water droplet formation and, under specific pressure and temperature conditions, as ice nuclei (IN) (Guerrieri et al., 2023). These processes can alter cloud optical and microphysical properties, enhance cloud reflectivity, affect cloud lifetimes, and increase the uncertainties in radiative transfer. Additionally, volcanic ice clouds can hide possible ash layers and pose a severe threat to aviation safety. Atmospheric transport models often struggle to account for these complex interactions, leading to uncertainties in plume evolution, trajectory forecasts, and deposition estimates. Furthermore, the absence of significant physical processes, dependence on empirical relations, and data from previous eruptions further contribute to substantial uncertainties in estimates of the erupted mass.

Over the past two decades, significant progress has been made in integrating remote sensing data into atmospheric transport models to enhance the forecasting of volcanic emissions and their dispersion. Satellite observations from both polar-orbiting and geosynchronous thermal infrared instruments have been used to retrieve ash mass loadings (Clarisse et al., 2010; Pavolonis et al., 2013; Prata and Prata, 2012). Additional sensors, including the Moderate Resolution Imaging Spectrometer (MODIS), Second Generation Spinning Enhanced Visible and Infra-Red Imager (SEVIRI), Atmospheric Infra-Red Sounder (AIRS), Ozone Monitoring Instrument (OMI), Multi-angle Imaging SpectroRadiometer (MISR), and CALIOP lidar on board the CALIPSO have provided valuable data on volcanic ash detection and retrievals (Eckhardt et al., 2008; Francis et al., 2012). A comprehensive discussion on the application of satellite remote sensing for volcanic ash monitoring in aviation hazard mitigation is provided by Prata (2009).

In addition, ground-based lidar networks, such as the European Aerosol Research Lidar Network (EARLINET), have played a crucial role in validating the accuracy of transport model outputs and improving dispersion simulations by providing high-resolution vertical profiles of volcanic aerosols (Pappalardo et al., 2004).

Advancements in atmospheric transport and dispersion modeling have further facilitated the integration of these observational datasets. Models like the Numerical

Atmospheric-dispersion Modelling Environment (NAME; Jones et al., 2007) (which is used operationally by the London Volcanic Ash Advisory Centre, or LVAAC), the Hybrid Single-Particle Lagrangian Integrated Trajectory (HYSPLIT) model (Stein et al., 2015), and the FLEXible PARTicle (FLEXPART) dispersion model (Eckhardt et al., 2008; Kristiansen et al., 2010, 2012, 2014; Stohl et al., 2011) have been extensively used for volcanic ash forecasting, often incorporating satellite and lidar data to refine model inputs and improve predictive accuracy.

The integration of remote sensing data into atmospheric transport models has been significantly advanced through inversion algorithms. In previous studies (Eckhardt et al., 2008; Kristiansen et al., 2010), inversion algorithms were developed using satellite column retrievals and tested to estimate the vertical distribution of sulfur dioxide (SO_2) emission rates for quasi-instantaneous volcanic eruptions such as the 2007 Jebel at Tair and the 2008 Kasatochi eruptions. Seibert et al. (2011) examined the uncertainties of the various configurations for the 2008 Kasatochi case study and expanded the method to estimate the uncertainty of the retrieved source emissions (a posteriori uncertainties).

The inversion algorithm was further used by Stohl et al. (2011) for volcanic ash emission rates as a function of altitude and time, while Kristiansen et al. (2012) improved the volcanic ash inversion techniques using various inputs to better constrain the 2010 Eyjafjallajökull eruption.

Amiridis et al. (2023) demonstrated that volcanic ash early warning systems can be significantly enhanced by the assimilation of Aeolus wind fields. Notably, these improvements are most pronounced over under-sampled geographical regions, such as the Mediterranean Sea, as volcanoes are often situated in remote areas lacking surface-based observation networks. Moreover, the study indicates that the positive effect of Aeolus wind data assimilation is more pronounced in the middle and upper troposphere (mostly between 7 and 15 km) compared to the lower troposphere. This may highlight under-sampling issues, since the in situ observations (like radiosondes) traditionally used for data assimilation exhibit lower vertical resolution in the upper troposphere (Rennie et al., 2021). Considering that volcanic ash plumes are typically injected into upper-tropospheric and lower-stratospheric heights, their transport is largely influenced by upper-tropospheric winds, hence accuracy in dispersion modeling is advanced from high-accuracy wind field assimilation.

Building on these advancements, our study further investigates improvements in ash emission estimations by developing an inversion method that integrates Aeolus wind data, ground-based lidar observations, and transport model simulations. This approach aims to enhance the accuracy of volcanic emission source terms and to reduce uncertainties in dispersion forecasting.

We specifically focus on the Etna eruption that occurred on 12 March 2021, coinciding with the investigations provided by Amiridis et al. (2023) and Kampouri et al. (2023). During this event, Aeolus had a close overpass to Etna, providing valuable observations around the volcano. Additionally, the transported volcanic plume was captured in the eastern region of the Mediterranean by the ground-based Polly^{XT} lidar system of the PANhellenic GEophysical observatory of Antikythera of the National Observatory of Athens (PANGEA-NOA) in Greece, downwind of the Etna volcano. This allows for direct comparisons of observations against forecasts, with and without the assimilation of Aeolus data, denoted as "w" and "w/o" Aeolus, respectively (as indicated in the studies by Amiridis et al., 2023; Kampouri et al., 2023).

2 The case of the Etna volcanic eruption of 12–14 March 2021

2.1 Volcanic activity

Mt. Etna in Italy, recognized as one of the most active volcanoes on Earth, has undergone significant volcanic activity, particularly since February 2021. During this period, the stratovolcano experienced numerous paroxysmal episodes, leading to frequent tephra and SO_2 emissions. A notable event occurred on 12 March 2021, marking one of the most powerful lava fountain episodes observed at the southeastern crater since 2020 (Calvari et al., 2021). The volcanic activity started with Strombolian-type eruptions at around 02:35 UTC, escalating in both frequency and intensity until 07:35 UTC, when surveillance cameras from the Istituto Nazionale di Geofisica e Vulcanologia, Osservatorio Etneo (INGV-OE) (Corradini et al., 2018; Scollo et al., 2019) captured the formation of a sustained lava fountain.

Throughout the paroxysmal phase, the eruptive column gradually reached a height of 9 km a.s.l. (Fig. 1). The variation in the eruption column was detected by the visual surveillance camera in the CUAD in Catania (ECV), calibrated by INGV-OE (Fig. 1). The volcanic plume drifted eastwards under the influence of the prevailing westerly winds dominant in the eastern Mediterranean region at the time. According to the Volcano Observatory Notice for Aviation (VONA) messages, the INGV-EO observatory (INGV, 2025; Corradini et al., 2018; Scollo et al., 2019) issued a red warning alert, from 06:18 to 08:44 UTC, on 12 March 2021, when the strongest ash emission was observed, while an orange alert was issued at 12:30 UTC when the lava fountain ceased, and the volcanic ash plume was dispersed into the atmosphere (Calvari et al., 2021). Additionally, the eruptive activity resulted in abundant tephra fallout, covering several towns on the eastern flank of the volcano crater, with a lava flow field expanding on the eastern and northeastern flank. In this study, the cloud heights reported by VONA are used as a priori information to initialize the volcanic ash dispersion simulations, conducted with the FLEXPART (flexible particle dispersion) Lagrangian model (Brioude et al., 2013; Pisso et al., 2019; Stohl et al., 2005). The FLEXPART ash trans-

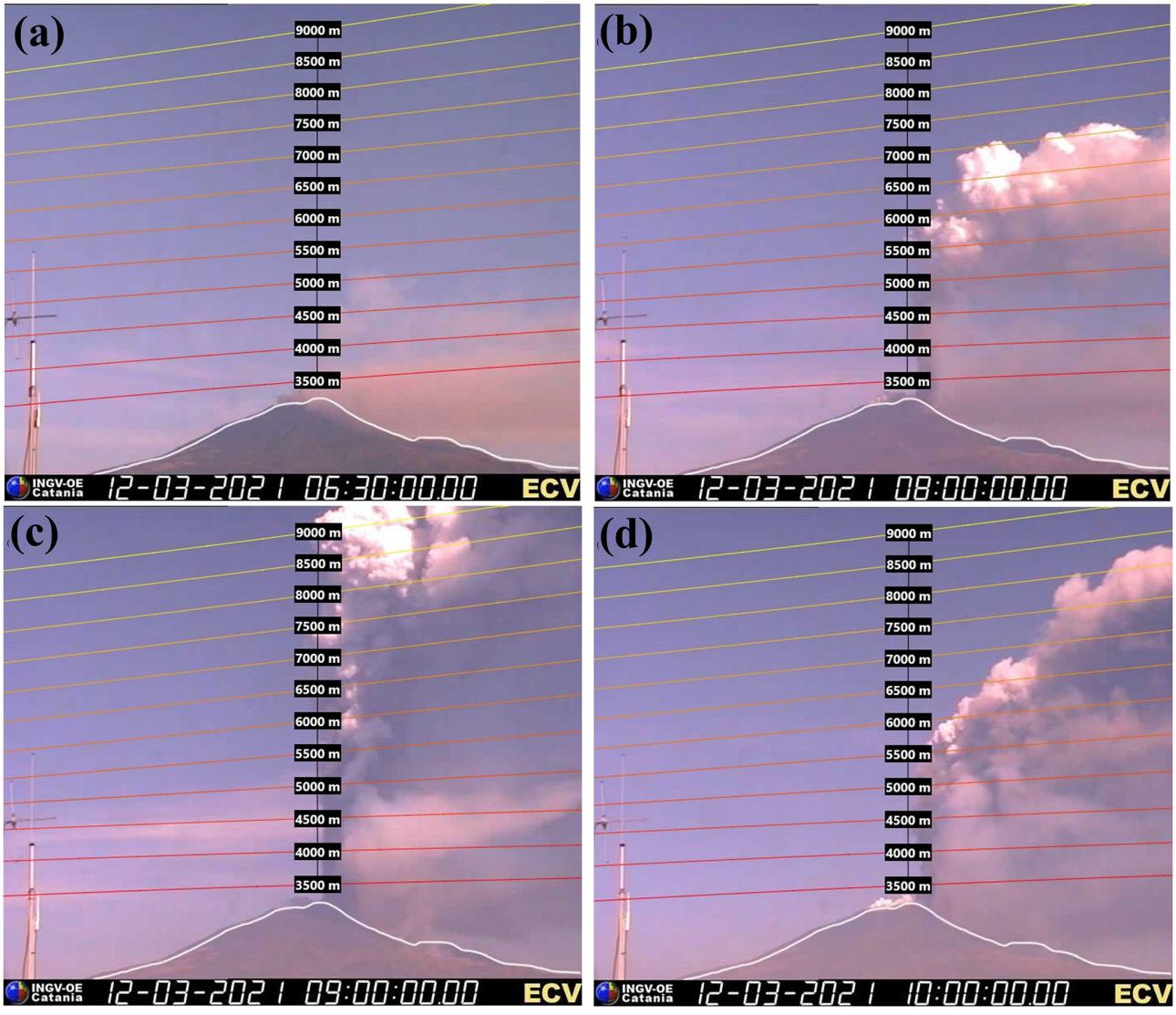

Figure 1. Etna activity on 12 March 2021 as seen from INGV-OE. Ash plume images from an ECV calibrated camera monitored the explosive volcanic activity between 5 and 9 km a.s.l. **(a)** Weak ash plume at 06:30 UTC, with an upper part aligning more vertically. **(b)** Strong vertical plume at 08:00 UTC, which shifted eastward. **(c)** Strong ash plume at 09:00 UTC, with a lower and more diluted cloud caused by the lava flow expanding eastward. **(d)** Decrease in the explosive activity after 10:00 UTC. Figures are taken from the INGV-OE automatic system described in Corradini et al. (2018) and Scollo et al. (2019).

port model is driven by wind fields simulated by the WRF regional meteorological model (version 4) (Skamarock et al., 2019), which, in turn, derives initial and boundary conditions from the European Centre for Medium-Range Weather Forecasts (ECMWF) Integrated Forecasting System (IFS) (ECMWF, 2021a) global model (for additional information, see Sect. 3.3).

3 Methods and data

The inverse method employed in this study to estimate volcanic ash emissions integrates a priori information on ash emissions, ground-based lidar observations, and simulations with a dispersion model, resulting in improved ash emission estimates. Figure A1 presents a schematic workflow outlining the methodology followed in this study, providing a clear overview of the steps involved in our approach. In this section, we describe the datasets and methods employed in the inverse modeling process.

3.1 PANGEA-NOA ground-based data (lidar Polly^{XT})

The PANGEA-NOA observatory established its first operations in June 2018 on the remote island of Antikythera, Greece. The atmospheric circulation pattern at PANGEA-

NOA favors the transport of air masses carrying an abundance of different aerosol types such as windblown Sahara dust, Etna volcanic aerosols, smoke from wildfires, and anthropogenic pollution from major cities. Hence, this coastal site constitutes an ideal place to study natural aerosols under the prevailing background conditions of the eastern Mediterranean.

The Mediterranean region, particularly its eastern basin, serves as a confluence of air masses originating from Europe, Asia, and Africa. In this region, anthropogenic emissions from large urban centers interact with natural emissions from the Saharan and Middle Eastern deserts, smoke from frequent wildfires, and volcanic particles from eruptions, notably from Mt. Etna and Icelandic volcanoes. Additionally, the atmosphere over the eastern Mediterranean contains background marine aerosols and pollen particles from oceanic and vegetative sources. Aerosols exert a variety of effects on the regional weather and climate, impacting solar radiation, visibility, and human health, and they pose significant concerns for aviation safety (WMO, 2024).

The eastern Mediterranean is characterized by a Mediterranean climate, with hot, dry summers and mild, wet winters. This seasonal variability is driven primarily by the interaction between mid-latitude westerlies and subtropical high-pressure systems (Lensky et al., 2018). During winter, the region experiences the frequent passage of extratropical cyclones originating from the North Atlantic and Mediterranean storm tracks, bringing precipitation and colder temperatures. In contrast, summer conditions are dominated by the expansion of the subtropical height, leading to stable atmospheric conditions and minimal rainfall (ECMWF, 2010).

Synoptic-scale circulation in the eastern Mediterranean plays a crucial role in shaping weather patterns and atmospheric dynamics. The atmospheric circulation over the eastern Mediterranean is dominated by persistent northerly and westerly winds, favoring the advection of volcanic products from Etna to Greece (Kampouri et al., 2020; Scollo et al., 2013). Research has identified several dominant synoptic types that influence the region, including cyclonic systems, anticyclonic patterns, and blocking heights (Rousi et al., 2014). These circulation patterns significantly impact the transport of aerosols, moisture, and pollutants, affecting regional air quality and climate variability. Furthermore, the region's proximity to large-scale circulation features such as the subtropical jet stream and the African monsoon system contributes to complex seasonal interactions (Lensky et al., 2018).

Currently, a Polly^{XT} lidar system (Baars et al., 2017; Engelmann et al., 2016) and a sun–sky photometer of CIMEL Electronique (Giles et al., 2019; Goloub et al., 2007) operate continuously at PANGEA-NOA to provide profiles and columnar aerosol properties with high accuracy and resolution.

Polly^{XT} is a multi-wavelength Raman polarization lidar with 24/7 remote operation capability. The system operates in 355, 532, and 1064 nm and is equipped with 12 detectors to measure light elastically and inelastically (at 387, 407, and 607 nm), backscattered from atmospheric constituents. Polarization capability also enables the detection and vertical separation of non-spherical (e.g., volcanic ash, dust) from spherical aerosols (e.g., smoke, pollution, marine particles).

The CIMEL sun–sky photometer measures direct solar and sky radiance at several wavelengths (340, 380, 440, 500, 675, 870, 1020, and 1640 nm) to derive column-integrated aerosol optical and microphysical properties (Dubovik et al., 2006).

Observations from both sensors are of strong interest for Pan-European and global networks such as the Aerosol, Clouds and Trace Gases Research Infrastructure (ACTRIS-RI), the European Aerosol Research Lidar Network (EARLINET), and the global AErosol RObotic NETwork (AERONET: https://aeronet.gsfc.nasa.gov/, last access: 27 June 2025). In all of these networks, measurements taken at PANGEA-NOA are submitted on a regular basis.

3.1.1 Ash mass calculations using remote sensing data

Volcanic ash mass estimates were derived from a combination of Polly^{XT} lidar measurements and sun photometer observations. First, the lidar measurements were averaged over the 3 h period when the volcanic layer was observed above Antikythera, and the standardized EARLINET algorithm Single Calculus Chain (SCC) (D'Amico et al., 2015) was used to derive the particle backscatter coefficient (β_p) and particle linear depolarization ratio (δ_p) profiles.

These profiles were then used to disentangle the contribution of large, non-spherical ash particles from the observed volcanic plume and to calculate the ash mass concentration with the POlarization-LIdar PHOtometer Networking (POLIPHON) method (Ansmann et al., 2012; Mamouri and Ansmann, 2017), tailored for Etna ash, as described in Kampouri et al. (2020).

More specifically, the following equation was used:

$$m_a = \rho_a \times c_{v,a}(\lambda) \times \beta_{p,a}(h,\lambda) \times S_{p,a}(h,\lambda), \quad (1)$$

where m is the mass concentration, a indicates an aerosol type, ρ represents the particle mass density (for volcanic ash particles, this is $2.6 \pm 0.6\,g\,m^{-3}$ following the study of Ansmann et al., 2011a), λ is the wavelength, $c_v(\lambda)$ is the so-called volume-to-extinction conversion factor (derived from sun photometer measurements), h is the height above ground, and $S_p(\lambda, h)$ is the ratio of the particle extinction to particle backscatter coefficient (lidar ratio).

As the m_a calculation is sensitive to the aerosol type, under the simultaneous presence of multiple aerosol components in the atmospheric column, a decomposition of the total particle backscatter coefficient β_p is needed prior to the mass concentration calculation. In POLIPHON, this decomposition is supported for up to two aerosol types, one exhibiting large particle depolarization ratio values (usually dust

Table 1. Parameters used for lidar profile decomposition and mass concentration calculation.

	ρ_α [µm cm^{-3}]	$c_{v,\alpha,532\,\mathrm{nm}}$	$\delta_{\mathrm{p},\alpha,532\,\mathrm{nm}}(h)$	$S_{\mathrm{p},\alpha,532\,\mathrm{nm}}(h)$ [sr]
Ash particles	2.6 ± 0.6	0.6 ± 0.1	0.36 ± 0.02	50 ± 10
Sulfates	1.5 ± 0.3	0.18 ± 0.02	0.05 ± 0.01	60 ± 20

or volcanic ash) and one that does not (marine, continental, or tropospheric smoke and their mixtures). To separate the contribution of the depolarizing ($\beta_{\mathrm{p,d}}(h,\lambda)$) and the non-depolarizing ($\beta_{\mathrm{p,nd}}(h,\lambda)$) aerosol component from the total particle backscatter coefficient, we apply the following equations:

$$\beta_{\mathrm{p,d}}(h,\lambda) = \beta_{\mathrm{p}}(h,\lambda) \times \frac{(\delta_{\mathrm{p}}(h,\lambda) - \delta_{\mathrm{p,nd}}(h,\lambda))(1+\delta_{\mathrm{p,d}}(h,\lambda))}{(\delta_{\mathrm{p,d}}(h,\lambda) - \delta_{\mathrm{p,nd}}(h,\lambda))(1+\delta_{\mathrm{p}}(h,\lambda))} \quad (2)$$

$$\beta_{\mathrm{p,nd}}(h,\lambda) = \beta_{\mathrm{p}}(h,\lambda) - \beta_{\mathrm{p,d}}(h,\lambda). \quad (3)$$

Polly$^{\mathrm{XT}}$ lidar signals are sensitive to aerosol particles in the radius range from about 50 nm to a few micrometers (Weitkamp, 2005). For FLEXPART, the size range considered for volcanic ash particles is between 5 and 21 µm in diameter and thus within the range that is detectable by Polly$^{\mathrm{XT}}$. Uncertainties in the ash mass concentration calculation using the POLIPHON method arise from the input parameter errors that propagate into Eq. (1) and are expected to be in the order of $\sim 40\,\%$ (Ansmann et al., 2011b). The technique has been validated against synergistic retrievals that combine multi-wavelength lidar and sun–sky radiometer observations (sensitive up to 15 µm in particle radius (Lopatin et al., 2013, 2021)) for dust and volcanic ash particles and has been found to perform well (Konsta et al., 2021; Wagner et al., 2013).

In Table 1, we summarize the values and uncertainties of the parameters used as input for the above. The lidar ratio of coarse-mode volcanic ash at 532 nm is reported to range between 40 and 60 sr in the literature (see for example Groß et al., 2012; Table 3 for particle extinction and backscatter values in Floutsi et al., 2023; and Gasteiger et al., 2011). For the fine-mode aerosols, we use a mean value of 60 sr, following the values reported in the literature for particles of a sulfuring nature (see for example Floutsi et al., 2023; Müller et al., 2007). We also account for a lidar ratio retrieval uncertainty of $\sim 30\,\%$ to capture the measurement range (Ansmann et al., 2012; Giannakaki et al., 2015; Groß et al., 2013). The particle density values ρ follow from the OPAC model for the coarse-mode mineral component and the water-soluble component for ash and sulfate particles, respectively (Hess et al., 1998; Koepke et al., 2015). For the water-soluble component, we assume values at a relative humidity of 0 %, which is considered representative of the altitudes of the volcanic layers. The coarse-mode component is not considered to be hydrophilic. Finally, the extinction-to-mass conversion factors cv are taken from Ansmann et al. (2011a) for ash and fine-mode particles, respectively.

3.2 Aeolus high-spectral-resolution lidar (HSRL) data

Aeolus, the wind mission of the European Space Agency (ESA), carried the world's first high-spectral-resolution Doppler wind lidar in space (Stoffelen et al., 2006; Straume-Lindner et al., 2021). Launched in August 2018, Aeolus's aim was to retrieve horizontal wind profiles in the troposphere and lower stratosphere. The mission's primary objective was to showcase this innovative technology in space to enhance weather forecasts and to advance our understanding of atmospheric dynamics, particularly in the tropics. Additionally, Aeolus aimed to contribute valuable insights into the intricate interactions between the atmospheric constituents, water cycles, and broader climate system (Rennie et al., 2021; Straume-Lindner et al., 2021). Aeolus wind data demonstrated notable quality and coverage, leading to substantial enhancements in NWP forecasts, particularly within the tropics and Southern Hemisphere. The improvement in wind forecast ranges from 0.5 % to 2 %, in terms of root mean square error, maintains a significant impact even in medium-range weather forecasting. The most substantial impact was observed at approximately 100 hPa in the tropics, particularly over the eastern Pacific Ocean. This is attributed, in part, to the tropics having a relatively limited coverage of high-quality radiosonde wind profiles. Additionally, the wind field in the tropics is less constrained by temperature information from other satellites (Rennie et al., 2021). Furthermore, Aeolus had the capability to retrieve aerosol and cloud profiles, offering valuable data for assimilation or evaluation in volcanic ash dispersion modeling. It is essential to note, however, that these retrievals face limitations due to the absence of a dedicated lidar channel for detecting cross-polarized light returns (with respect to the emitted radiation). This absence is particularly crucial for capturing the backscattered light from non-spherical particles like volcanic ash. Consequently, caution is advised when utilizing Aeolus observations in such cases. Despite this limitation, the Aeolus mission demonstrated its efficacy in enhancing wind forecasts, particularly over under-sampled regions, such as the tropics (Rennie et al., 2021). Similarly, Aeolus can be used over under-sampled remote areas with active volcanoes, contributing to improved simulations of volcanic ash dispersion following eruptions.

Table 2. Configuration of the PP schemes for the WRF-ARW simulations.

PP	Schemes	References
Microphysics (MP)	Thompson	Thompson et al. (2008)
Surface layer (SFL)	Monin–Obukhov (Janjic Eta)	Janjic (2002)
Planetary boundary layer (PBL)	Mellor–Yamada–Janjic (MYJ)	Janjic (2003)
Cumulus parameterization (CUM)	Tiedtke	Zhang et al. (2011)
Longwave and shortwave radiation (RAD)	Rapid radiative transfer model (RRTM)	Iacono et al. (2008)
Land surface (LSM)	NOAH	Chen and Dudhia (2001)

3.3 FLEXPART-WRF model setup

To perform meteorological simulations over the study region of the eastern Mediterranean, the Advanced Research WRF model (version 4) (Skamarock et al., 2019) is used. The spatial resolution of the model is 12 km × 12 km for a total of 351 × 252 grid points and 31 vertical levels (up to 50 hPa). The simulation period starts on 12 March 2021 at 00:00 UTC (6 h earlier than the FLEXPART runs to accommodate the model's 12 h spin-up) and ends on 14 March 2021 at 18:00 UTC, with hourly outputs. Table 2 summarizes the physics parameterization (PP) schemes for the WRF-ARW simulations.

In the context of this study, two versions (ECMWF, 2021a) of the initial and boundary condition fields from the IFS were utilized. These fields, provided at a spatial resolution of 0.125° × 0.125°, with 137 vertical model levels, serve as inputs for the WRF-ARW regional model. One version incorporates assimilated Aeolus Rayleigh-clear and Mie-cloudy horizontal line-of-sight (HLOS) L2B wind profiles (referred to as the "w" Aeolus experiment), while the other version is without Aeolus data (referred to as the "w/o" Aeolus experiment). The initial conditions without Aeolus assimilation adhere to the model setup utilized in the observing system experiments (OSEs) conducted by Stoffelen et al. (2006).

The WRF-ARW runs rely on initial and boundary conditions generated from ECMWF-IFS, with boundary conditions updated at 6-hour intervals. Sea surface temperature (SST) analysis data, obtained from the Copernicus Marine Environment Monitoring Service (CMEMS) at a spatial resolution of 1/12° supplement these simulations. The WRF-ARW model configuration utilized in this study is consistent with that employed in the study of Amiridis et al. (2023).

The volcanic ash plume transport simulations were done with the Lagrangian particle dispersion model FLEXPART (Brioude et al., 2013; Pisso et al., 2019; Stohl et al., 2005) in a forward mode. These simulations rely on hourly meteorological fields from the WRF-ARW model, initiated with IFS datasets. The use of 1-hourly WRF meteorological fields at a 12 km × 12 km spatial resolution allows for a more detailed representation of the volcanic plume dispersion. The initial simulations, in which we used an a priori emission profile for the eruption emissions taken from VONA alerts (from now on referred to as "a priori volcanic ash plume transport"), were initiated at the reported start time of the eruption at 07:00 UTC on 12 March 2021 and were completed at 00:00 UTC on 14 March 2021, with a total of 100 000 particles released in each forecast. The model layers were divided into 18 layers with 1 km vertical resolution in the range extending from 1 to 18 km above ground level (a.g.l.). We estimate the a priori mass eruption rate (MER) for ash particles following Mastin et al. (2009) and Scollo et al. (2019) by inverting the observed plume heights over the Etna summit crater from the VONA reports and field observations, as observed by the INGV observatory, using the 1D plume model of Degruyter and Bonadonna (2012). The initial injection height in the model is set to the altitude of the Etna summit craters (3.3 km a.s.l.) up to 9 km a.s.l., based on the VONA reports (Corradini et al., 2018; Scollo et al., 2019) and field observations. Also, the gravitational particle settling (Näslund and Thaning, 1991) was determined assuming spherical particles with a density of 2450 kg m^{-3}. The particle density value used in the FLEXPART model differs slightly from the density used in Table 1 (2.6 ± 0.6 g cm^{-3}) due to differences in shape assumptions, size distributions, and literature sources referenced in various calculations. The size distribution of volcanic ash particles was described using four size bins (3, 5, 9, and 21 µm in diameter), as these cover the size distribution relevant to long-range transport (≤ 25 µm diameter) (Beckett et al., 2022; Dacre et al., 2011; Durant et al., 2010).

To derive the source–receptor relationships (SRRs), the FLEXPART-WRF model was used, once again in a forward mode (see Appendix A, Fig. A2), considering the same four ash size bins as those used in the a priori volcanic ash plume transport. The SRR model data, which represent all potential dispersion scenarios of the ash plume, are compared with the lidar retrievals at PANGEA-NOA. For each grid point in the considered domain, the FLEXPART ash column loadings released from one particular emission time and height are matched with the corresponding time and grid point of the lidar ash mass retrieval.

The FLEXPART SRRs were driven by the same hourly meteorological fields from the WRF-ARW model, utilizing both control and assimilated datasets (ECMWF, 2021) to quantitatively evaluate the impact of data assimilation. Subsequently, these SRRs were used to initialize the inversion al-

gorithm, constrained by the Polly^{XT} ground-based lidar measurements of volcanic particles.

It was assumed that the ash emissions occurred between the ground and 16 km a.g.l. over the Etna volcano. The total height range was discretized into 79 layers of 200 m thickness. For each layer, 150 000 unit mass particle traces were uniformly released along a vertical line source every 2 h (from 04:00 to 06:00 UTC until 12:00 to 14:00 UTC). Additionally, the model layers were divided into 74: 70 layers between 200 m and 14 km, with a vertical resolution of 200 m; 3 layers between 14 and 16 km a.g.l. (per 1 km); and another layer from 22 to 50 km a.g.l. These model-derived column values represent source–receptor relationships, since they were obtained with a unit mass as the source. The actual mass released at each level is determined through the inversion. Following the inversion, a single, longer "posteriori" simulation over the period 12 to 14 March 2021 was made, releasing 200 000 particles according to the estimated emission profile. The output from this simulation was produced at the same vertical and horizontal resolution as the a priori FLEXPART simulation.

3.4 Inversion algorithm

The inversion method employed here for ash source estimations is based on a cost function minimization approach. Similar work has been done by Eckhardt et al. (2008), Kristiansen et al. (2010), and Stohl et al. (2011). In these studies, an inversion algorithm was developed to calculate the vertical distribution of sulfur dioxide and the ash emission rates for instantaneous volcanic eruptions. Satellite retrievals, typically of ash column loading, have been combined in those analyses with VATDM simulations using inversion techniques to provide time-evolving estimates of these significant quantities.

In satellite retrieval techniques, numerous advantages exist where estimates of ash cloud top height and ash column loading are typically available (Francis et al., 2012; Pavolonis et al., 2013). Additionally, MER can be estimated through empirical relationships under specific assumptions, which are especially useful when satellite images are unavailable or limited, such as during the early stages of an eruption (Pouget et al., 2013; Prata et al., 2022). However, direct retrievals of the vertical distribution within the eruption column are not feasible. Ground-based and airborne radar observations, which are sensitive to larger particles and can penetrate optically thick plumes, provide a complementary source of information to retrieve near-source plume properties such as mass eruption rate and column height.

The present study brings together (i) the inverse modeling by initiating the inversion simulations with mass concentrations derived from ground-based lidar observations downwind, combined with the source–receptor relationships calculated from the FLEXPART-WRF model, and (ii) the integration of Aeolus meteorological wind fields (ECMWF, 2021a) into the FLEXPART-WRF model (for more detail, see Sect. 3.3). The overarching goal is to optimize both the vertical emission distribution and the ash emission rates near the source, following the volcanic eruption. From the inversion scheme, a total ash emission profile of the eruption is obtained, which can be utilized to generate robust ash forecasts constrained by lidar observations.

We perform the inversion using a Bayesian approach to provide the best estimate of the emissions profile for fine ash (with particles 3, 5, 9, and 21 µm in diameter) that can be transported over long distances. We follow the general concept of source–receptor relationships (Seibert and Frank, 2004), where the relations between each measurement and a potential source of the emission is calculated (here using FLEXPART-WRF) and stored as the source–receptor matrix (SRM) for each vertical level and for four ash size bins (as described in Sect. 3.3). The $n = 79$ unknowns (source elements) are put into a state vector $\boldsymbol{x}$ while the observed values m are put into a vector $\boldsymbol{y}_o$, where the subscript "o" stands for the Polly^{XT} lidar observations. Then, the state vector can be calculated from the inversion of a forward model M that connects $\boldsymbol{y}_o$ and $\boldsymbol{x}$, as follows:

$$\boldsymbol{y}_o = M(\boldsymbol{x}) + e_y, \tag{4}$$

implying a linear relationship in which $\boldsymbol{y}_o$ is a vector of spatiotemporal lidar measurements; M is the $n \times m$ SRM calculated by FLEXPART-WRF, describing the sensitivity of each observation to a unit release rate; e_y represents lidar measurement errors, which are not accounted for in the algorithm; and $\boldsymbol{x}$ is the ash emission vector to be estimated. $M(\boldsymbol{x})$ is equivalent to running a VATDM with $\boldsymbol{x}$ as the input release profile. Since M is calculated using such a model, it inherits the biases that are inevitable in VATDMs. As a result, it may diverge from the true dispersion and may not necessarily align with the observations on the left-hand side of Eq. (4), even if it is the true release profile (Fang et al., 2022). Given that the problem is underdetermined, the solution of the linear inverse problem in Eq. (4) is not straightforward, and further assumptions are needed.

The most common are assumptions imposed on the unknown emission vector $\boldsymbol{x}$ such as the non-negativity of its elements, smoothness of the emission (Fang et al., 2022), or measurement/emission sparsity (Li et al., 2018) (e.g., the assumption that the emission element remains zero unless other evidence is present in measured and modeled data). Under these assumptions, the problem in Eq. (4) can be solved by minimizing the distance between the left and the right sides of the equation. To enhance the stability of the inversion outcome, a priori emissions are also used, representing our best estimate of $\boldsymbol{x}$ before the observations are made (see Sect. 3.4.1). Including an explicit a priori source vector $\boldsymbol{x}^a$, we can express the equation as follows:

$$M(x - \boldsymbol{x}^a) \approx \boldsymbol{y}_o - M\boldsymbol{x}^a, \tag{5}$$

and as an abbreviation

$$M\tilde{\boldsymbol{x}} \approx \tilde{\boldsymbol{y}}. \quad (6)$$

The inversion scheme presented here is done by minimizing a cost function C, which comprises the following system of equations:

$$C_1 = \boldsymbol{y}_o - M^T\boldsymbol{x} \quad (7)$$
$$C_2 = \boldsymbol{x} - \boldsymbol{x}^a \quad (8)$$
$$C_3 = \epsilon D\boldsymbol{x}. \quad (9)$$

C_1 quantifies the difference between the modeled data and the observations, C_2 is the deviation from the a priori estimations, and C_3 imposes a smoothness regularization term.

The cost function C first calculates the misfit C_1 between the profiles at the receptor points, as observed by the lidar ($\boldsymbol{y}_o$) and the data as modeled by FLEXPART ($M^T\boldsymbol{x}$).

The second term C_2 (Eq. 8) accounts for the difference between the a posteriori estimates of the emission rates $\boldsymbol{x}$ and the a priori estimates x^a. (For details on the calculation of the a priori vector, see Sect. 3.4.1.) To enforce smoothness in the vertical profile of emissions, a regularization parameter C_3 is introduced, derived from a discrete second-order difference operator D (Eq. 9). D represents a tridiagonal matrix where the main diagonal elements are equal to -2, elements of the diagonals above and below are equal to 1 (discrete representation of the second derivative), and ϵ is a regularization parameter that determines the weight of this smoothness constraint relative to the other two terms.

The final mass emission rates are obtained by minimizing the total cost function C using a standard optimization routine with the a priori emission rates as the initial guess. This approach ensures that the calculated ash emission rates are consistent with both the observed data and the a priori emission estimates, while also favoring a smooth vertical distribution of emissions.

The inversion scheme presented in this study is not limited to Mt. Etna but can be applied to other volcanic eruptions worldwide, provided that suitable observational data are available. The methodology relies on ground-based lidar measurements, dispersion modeling (FLEXPART-WRF), and an inversion algorithm to estimate volcanic ash emissions. Therefore, it can be adapted to different volcanic settings where lidar observations or other remote sensing data like satellite-based lidars (CALIPSO, EarthCARE) and geostationary satellites (SEVIRI) are available to constrain the source term. Additionally, the approach can be extended to a regional or global scale by integrating multiple observation sites from lidar networks such as ACTRIS/EARLINET or incorporating additional satellite data. This would allow for improved ash emission estimates for various volcanic eruptions worldwide. Furthermore, the use of high-resolution wind field data (such as Aeolus or future wind lidar missions) can enhance the accuracy of dispersion forecasts in different geographic regions (possibly lacking sufficient information from radiosondes), making the methodology widely applicable for volcanic ash monitoring and forecasting.

3.4.1 A priori source emissions x^a

To constrain the variability of the retrieved parameters and to enhance the stability of the inversion outcome, a priori emissions are also used in the inversion scheme. We determine the a priori MER for ash particles following the approach outlined by Scollo et al. (2019) by inverting the observed plume heights over the Etna summit crater from VONA reports and field observations as observed by the INGV observatory, using the 1D plume model (Degruyter and Bonadonna, 2012) as described in Sect. 3.3. Additionally, the London VAAC employs the same empirical relationship between observed plume heights and eruptive mass, as proposed by Mastin et al. (2009), assuming a uniform vertical ash distribution.

The column heights of the ash plume from 12 March 2021 were obtained from the ECV calibrated camera operated by INGV-OE (Calvari et al., 2021; Corradini et al., 2018; Scollo et al., 2019) during the time period of 06:30 to 10:30 UTC (see Table A1). The ash plume height reached up to 9.0 km a.s.l. In order to calculate the a priori emissions, the data were resampled at $\sim$2 h intervals, specifically at 06:00 (from 06:30 to 07:45 UTC), 08:00 (from 08:00 to 09:45 UTC), and 10:00 UTC (from 10:00 to 10:30 UTC). During the initial hours of the eruption (06:30–07:45 UTC), the ash plume was weak (Fig. 1a and Table A1) with an average column injection height of 5.8 km, resulting in an estimated MER of approximately 12 000 kg s^{-1} according to the equation by Mastin et al. (2009) (Table 3). After 07:45 UTC, a stronger plume formed, extending vertically above the vent (Fig. 1b and Table A1). The ash plume exceeded the ECV camera field of view (e.g., more than 9.0–9.5 km a.s.l.) and was particularly strong between 08:00 and 09:45 UTC (Fig. 1c and Table A1). The MER during this period averaged 58 800 kg s^{-1}, with a mean plume height of 10 km a.s.l. The standard deviation of the mean MER indicates considerable inconsistency in the emissions, as the MER can change rapidly during an eruption due to fluctuations in the eruptive dynamics, such as the collapse of the eruption column (Table 3). The ash plume height began to decrease several minutes after the lava fountain ceased (Fig. 1d and Table A1), with its disappearance becoming evident only after 10:15 UTC (Fig. 1d). The MER during this phase (10:00–10:30 UTC) was approximately 6300 kg s^{-1} (Table 3). The maximum plume elevation was not recorded by the ECV camera due to its limited field of view (approx. 9.0–9.5 km a.s.l. as noted by Scollo et al., 2014). However, according to SEVIRI aboard the geostationary Meteosat Second Generation satellite, the volcanic ash cloud top height (ACTH) between 08:15 and 08:45 UTC was estimated at 11.5 km a.s.l. (Calvari et al., 2021). This higher SEVIRI-

Table 3. A priori source vector $\boldsymbol{x}^{a}$.

Time (UTC)	Mean column height (m)	Mean mass eruption rate (MER) ($kg\,s^{-1}$)	Standard deviation (SD) of mean MER ($kg\,s^{-1}$)
12 Mar 2021 06:00:00	5850	12 000	10 200
12 Mar 2021 08:00:00	10 000	58 800	35 000
12 Mar 2021 10:00:00	5300	6320	5120

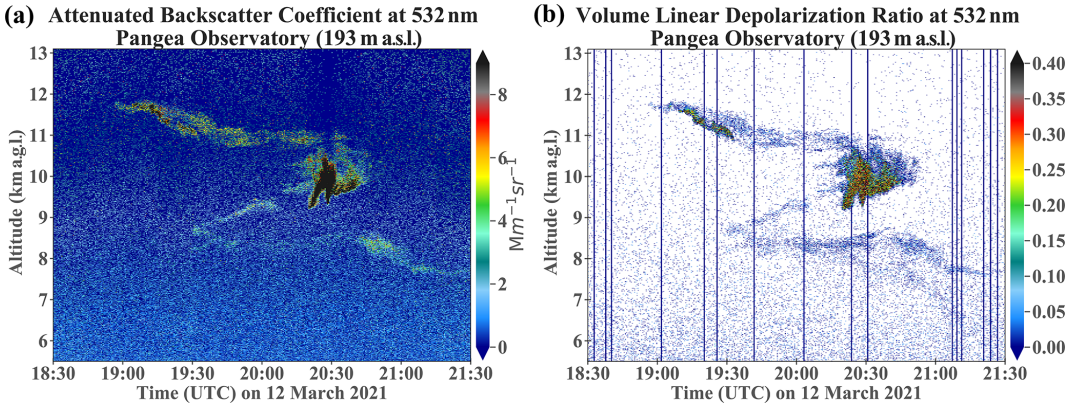

Figure 2. **(a)** The time–height curtain plot of the attenuated backscatter coefficient and **(b)** the volume linear depolarization ratio at 532 nm based on Polly^{XT} lidar observations at the PANGEA-NOA observatory during 12 March 2021 (18:30 to 21:30 UTC). Station elevation is at 193 m a.s.l. Altitude heights are given in kilometers above ground level. The blue vertical lines in panel **(b)** indicate negative values, which arise due to a low signal-to-noise ratio (SNR) of the measurements, and they are masked before data averaging and final retrievals.

derived plume height was used in the calculations for the a priori ash emissions during this time window, as it provides a more accurate representation of the plume height at the peak of the eruption (see Appendix Table A1).

4 Results

On 12 March 2021 the Etna volcanic plume was captured over the PANGEA-NOA observatory by the Polly^{XT} lidar system. A 3 h time window from 18:30 to 21:30 UTC was selected to calculate the aerosol optical properties using the Raman method (Ansmann et al., 2011b). This time window was chosen based both on the lidar observations and the FLEXPART simulations, which also indicated the presence of ash particles over the PANGEA-NOA station. Figure 2 shows the time–height evolution of the Polly^{XT} lidar measurements, depicting a dense aerosol layer between 8 and 12 km a.g.l., with the majority of the ash plume (large, depolarizing aerosols) confined in the altitudes between 9 and 11 km approximately 11 h after the eruption (18:30–21:30 UTC). The layer is associated with volcanic ash advection from Etna, as indicated by the high-volume linear depolarization ratios (40 %–50 % at the center of the plume), which are typical of non-spherical volcanic ash particles (Gasteiger et al., 2011; Groß et al., 2013; Tackett et al., 2023; Wiegner et al., 2012) (Fig. 2b).

To further analyze the volcanic plume distribution, Fig. 3 presents the mass eruption rates in $kg\,s^{-1}$ for both the a priori (represented by circles) and a posteriori (represented by stars) values, plotted as a function of ash plume height (km a.s.l.) and eruption time (UTC). The a posteriori ash particle emissions in the "w" Aeolus simulation (Fig. 3a and b), obtained through the inversion scheme presented herein, were used as input for a new FLEXPART forward run. As discussed in Sect. 3.4.1, the a priori MER (Fig. 3a and b) for ash particles was determined using the approach outlined by Scollo et al. (2019). The a priori MER was obtained by inverting the observed plume heights from the VONA reports, based on data collected by calibrated cameras operated by the INGV-EO observatory. The ash plume's disappearance becomes noticeable only after 10:15 UTC (Fig. 1d).

The a priori MER values represented by circles exhibit significant variability throughout the eruption period on 12 March 2021, between 06:30 and 10:30 UTC. Peak MER values approaching 80 000 $kg\,s^{-1}$ are observed at approximately 12 km altitude between 09:30 and 09:45 UTC. Additionally, notable peaks occur at lower altitudes between 08:15 and 09:00 UTC, where MER values reach approximately 45 000 $kg\,s^{-1}$ at around 9 km altitude (Fig. 3a and b).

In contrast, the a posteriori MER values, denoted by stars, display a more constrained and consistent pattern, with lower magnitudes across most altitudes and times with respect to the a priori estimates. The maximum a posteriori MER reaches approximately 45 000 $kg\,s^{-1}$ at an altitude of

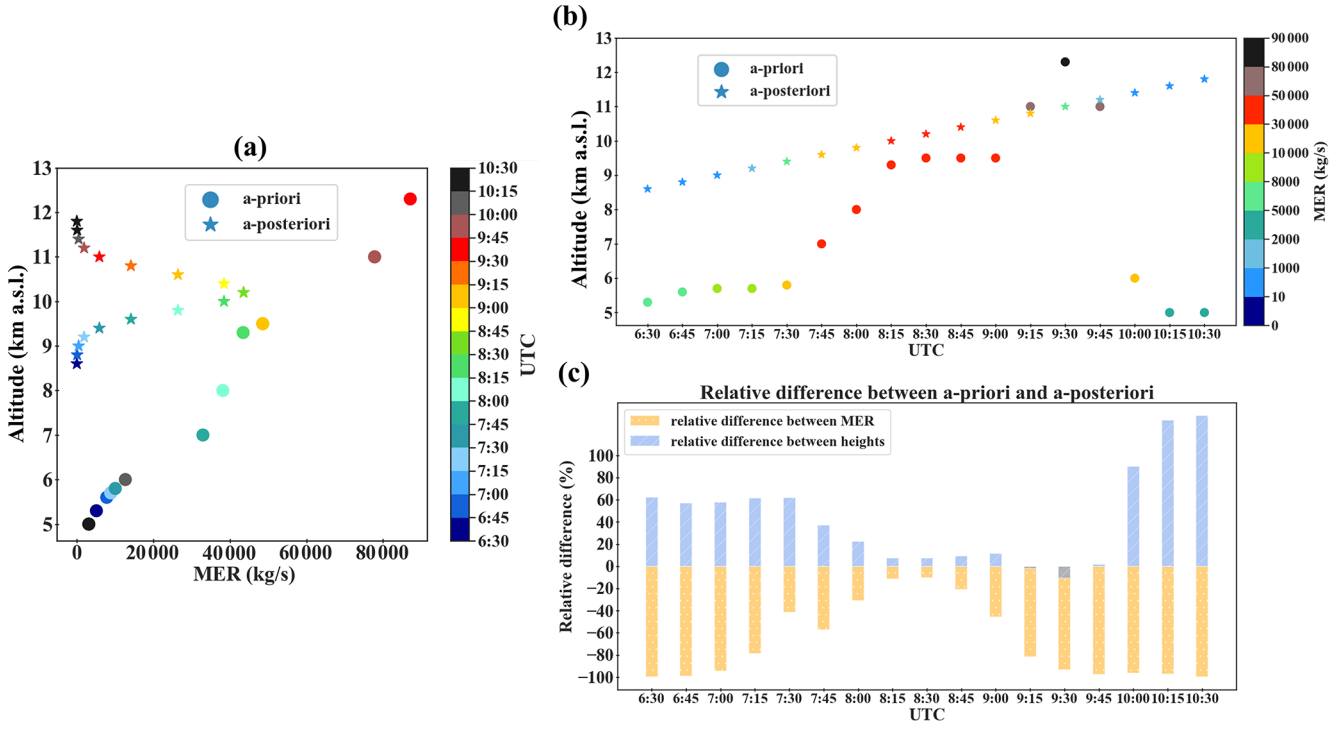

Figure 3. A priori and a posteriori ash emissions. **(a)** Comparison of temporally averaged vertical profiles of ash emissions used a priori (circles) and obtained a posteriori by the inversion (stars). The color bar indicates the corresponding times of eruption (on 12 March 2021, from 06:30–10:30 UTC), each color representing a specific time. **(b)** A priori (circles) and a posteriori (stars) MER (unit $\mathrm{kg\,s^{-1}}$) as a function of altitude (km) and time (UTC) on 12 March 2021 from 06:30 to 10:30 UTC. The color bar indicates the corresponding MER values (from 0 to 90 000 $\mathrm{kg\,s^{-1}}$), each color representing a specific MER range. The time axis reflects the period during which the ash plume was recorded by the ECV calibrated camera (06:30–10:30 UTC). **(c)** Relative differences (%) between a posteriori and a priori for ash emissions (orange columns) and plume height (blue columns) as a function of time (UTC). All heights are given in kilometers above sea level.

10.5 km, occurring between 08:15 and 08:45 UTC (Fig. 3a and b).

The eruption dynamics involve a complex evolution of the volcanic plume, with phases of rising and collapsing. However, this dynamic behavior is not explicitly resolved in the a posteriori simulations, which do not capture rapid fluctuations in plume height and intensity. Instead, the inversion algorithm adjusts the a posteriori MER at each altitude over time, dynamically increasing or decreasing emission rates to achieve the best agreement with available observations. The most significant refinement occurs between 08:15 and 08:45 UTC, within the 8–12 km altitude range, where lidar observations provide direct constraints on the plume's vertical structure. As a result, the inversion optimizes the emission estimates primarily within this altitude range, ensuring the highest degree of agreement between observed and a posteriori emissions.

A notable distinction between the two sets of emission estimates is the greater spread of the a priori emissions across a wider range of altitudes, with values often exceeding those of the a posteriori emissions. This is especially evident at lower altitudes (below 7 km) (Fig. 3b and c), where relative differences range between 40 % and 80 % from 06:30 to 07:45 UTC. These differences suggest an overestimation of the initial a priori emissions obtained by inverting observed plume heights from the VONA reports, compared to the ash emissions derived from the inversion scheme (Fig. 3c).

On the other hand, the a posteriori MER values present a more refined and clustered distribution between 8 and 12 km altitude (Fig. 3a), indicating a more constrained and likely more accurate estimation of ash emissions. This contrast is particularly evident when compared to the more scattered and variable a priori estimates.

Between 10:00 and 10:30 UTC, both a priori and a posteriori estimates indicate a distinct decline in MER, with values dropping below 10 000 $\mathrm{kg\,s^{-1}}$ at lower altitudes ($\sim$ 5 km). During this period, the relative differences between plume height and MER exceed 80 %, highlighting the divergence between the initial and adjusted estimates (Fig. 3c).

Regarding the ash plume height, the a posteriori estimates consistently indicate higher altitudes compared to the a priori estimates, a discrepancy potentially attributed to the limited field of view of the calibrated camera from the INGV-EO observatory. The camera's restricted range (approximately 9.0–9.5 km a.s.l., as noted by Scollo et al., 2014) may have failed

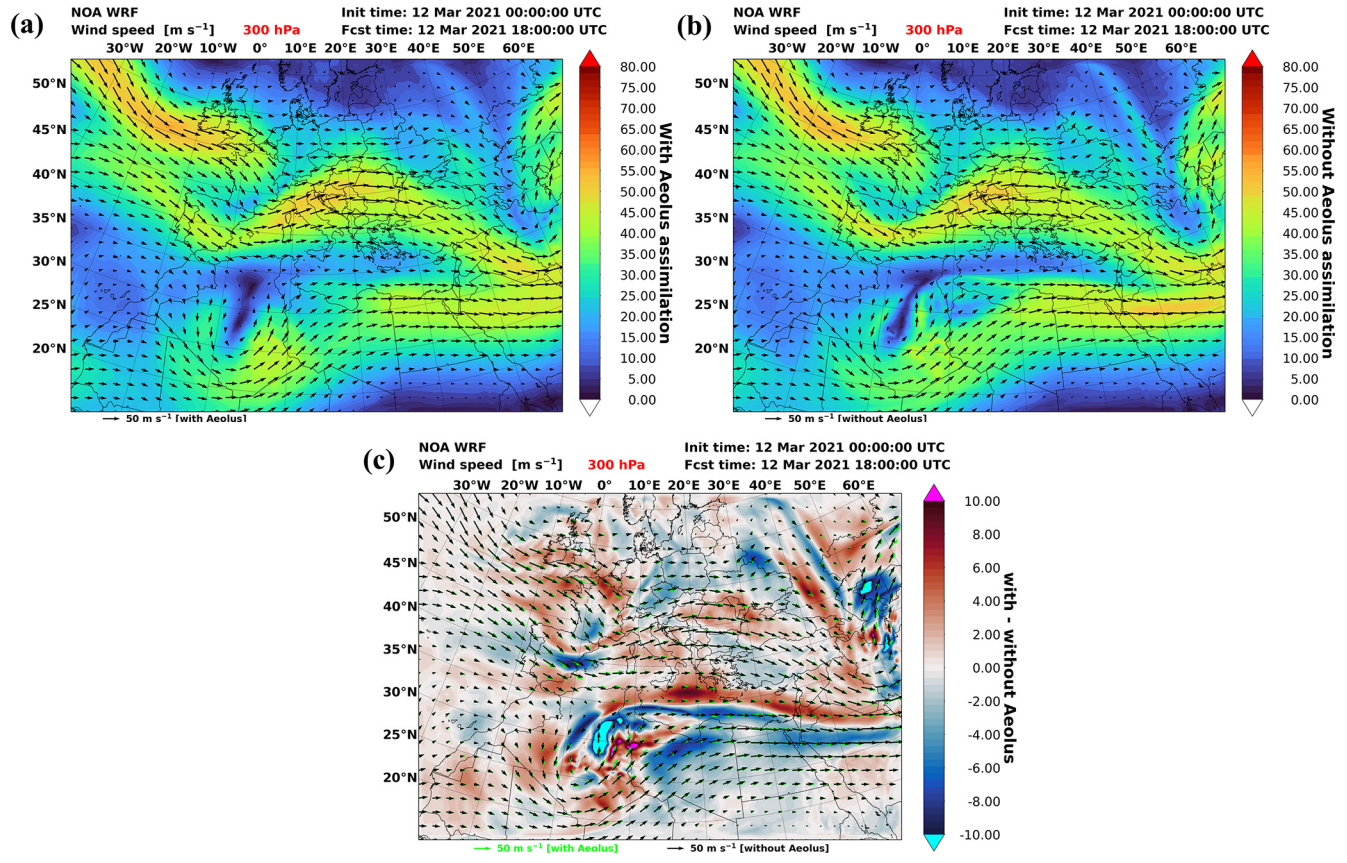

Figure 4. Wind speed ($m s^{-1}$) in WRF 18 h forecasts. Horizontal winds **(a)** "w" Aeolus assimilation, **(b)** "w/o" Aeolus assimilation, and **(c)** wind speed differences ("w" − "w/o" Aeolus assimilation) at 300 hPa (∼ 9.6 km).

to capture the full extent of the plume, leading to underestimations in the a priori estimates.

Additionally, Calvari et al. (2021) further indicate that the observed plume column altitudes predominantly range between 6 and 9 km, which is the upper limit of the INGV-OE camera system. As a result, column heights exceeding 9 km a.s.l. are likely limited, contributing to differences between a priori and a posteriori estimates.

The relative differences between the two estimates are notably smaller, ranging from 10 % to 40 % between 08:00 and 09:00 UTC (Fig. 3c), suggesting a reasonable agreement between the a priori and a posteriori assessments for both emissions and column heights during this time window of the eruptive phase.

This improvement in the a posteriori profile underscores the efficacy of the inversion algorithm in producing a more reliable representation of the vertical distribution of the ash emissions by improving the precision of eruption source parameters. The a posteriori MER profile alignment with the observational data suggests that this method provides a robust and realistic assessment of ash emissions, particularly in the critical altitude range where volcanic plumes typically occur (Degruyter and Bonadonna, 2012; Mastin et al., 2009; Scollo et al., 2019).

The transport and dispersion of volcanic ash particles are strongly influenced by upper-air circulation patterns, which play a crucial role in determining the trajectory and lifetime of the volcanic plume. To assess the sensitivity of the volcanic ash transport to the driving meteorology, two simulations were performed using the WRF regional model during the study period. These simulations were driven by two versions of the ECMWF-IFS global model: one incorporating the Aeolus wind profile assimilation ("w") and one without the Aeolus assimilation ("w/o") (see Sect. 3.3). To evaluate the influence of upper-level circulation on volcanic ash transport, wind maps at 100, 200, 300, and 500 hPa were generated for the period of significant volcanic activity (Figs. A3–A5).

Given that lidar observations estimated the volcanic plume's center of mass at approximately 10 km, the analysis primarily focused on the 300 hPa level (∼ 9.6 km), which closely corresponds to this altitude (Fig. 4). Analyzing the WRF regional model wind vectors at upper-tropospheric levels (300 hPa, ∼ 9.6 km) at 18:00 UTC (approximately 11 h after the Etna eruption), the general atmospheric circulation

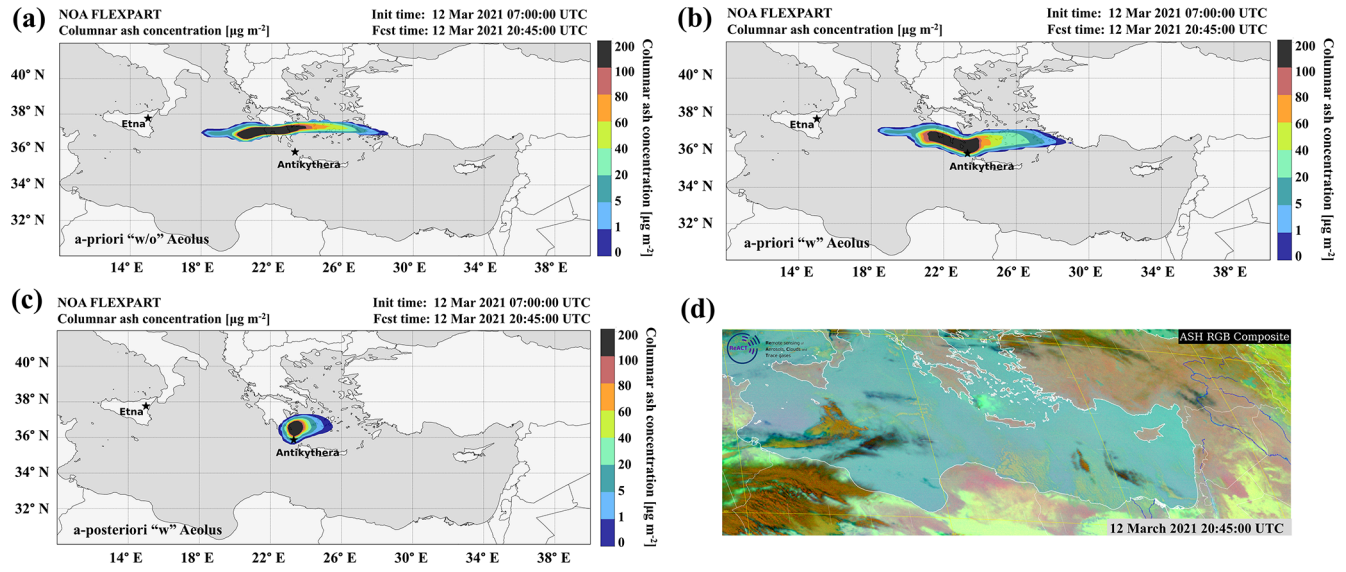

Figure 5. FLEXPART simulations of volcanic ash. **(a)** A priori ash column loading ($\mu g\,m^{-2}$), using the meteorological fields "w/o". **(b)** "w" Aeolus wind assimilation. **(c)** A posteriori ash column loading ($\mu g\,m^{-2}$), using meteorological fields "w" (12 March 2021, 20:45 UTC). **(d)** EUMETSAT Meteosat-11 Ash (RGB-MSG-0-degree), product of the ash plume derived from the Spinning Enhanced Visible and InfraRed Imager (SEVIRI) during paroxysmal activity at Mt. Etna on 12 March 2021. Composite thermal IR (8.7, 10.8, 12 wavelengths) satellite image from the SEVIRI captures the volcanic ash plume about 11 h after the start of the eruption above the PANGEA-NOA station, at Antikythera island in Greece on 12 March 2021 at 20:45 UTC (SEVIRI data are taken from the EUMETSAT data portal; https://view.eumetsat.int/productviewer?v=default, last access: 27 June 2025).

remained predominantly zonal over the Mediterranean, with westerly winds prevailing throughout the troposphere. Over the Anatolian Plateau and the eastern Mediterranean Sea, these winds transition into northwesterlies, favoring the direct transport of the Etna plume towards Greece and the eastern Mediterranean.

A comparison of the two simulations ("w" and "w/o" Aeolus assimilation) indicates that the overall atmospheric pattern remains consistent, with the subtropical and polar jet streams dominating the circulation. However, notable differences in wind speed are evident, as highlighted in the wind speed difference map for the WRF 18 h forecast (Fig. 4).

The color shading in Fig. 4c illustrates the differences between the two WRF runs on 12 March 2021 (18:00 UTC). This comparison indicates the significant strengthening of winds at 300 hPa when Aeolus wind profiles are assimilated (Fig. 4c), with maximum difference values reaching approximately $8\,m\,s^{-1}$. Additionally, slight differences in wind vector direction ("w" Aeolus (green) and "w/o" Aeolus (black)) are observed, particularly over the Ionian Sea (from W to NW) and the eastern Mediterranean between Crete and Cyprus (from WNW to NW), where the two jet streams merge.

Similar wind speed tendencies are observed at 200 hPa (Fig. A4). In contrast, at 500 hPa (Fig. A5), the influence of Aeolus assimilation is less pronounced, indicating that the most significant differences occur at higher altitudes where jet stream dynamics dominate.

At 100 hPa (Fig. A3), a strong westerly jet stream is evident across Europe and North Africa, indicating fast-moving winds that could contribute to the long-range transport of volcanic particles. The corresponding wind speed difference map (Fig. A3c) shows high differences mainly along the jet stream axis, suggesting that Aeolus assimilation plays a crucial role in improving the representation of high-altitude wind fields critical for long-range ash transport.

These findings highlight the importance of accurate upper-air circulation representation in volcanic ash transport modeling. The inclusion of Aeolus wind profiles in the ECMWF-IFS model leads to a more refined depiction of wind patterns, particularly at upper tropospheric and lower stratospheric levels, which are crucial for accurately forecasting the dispersion of volcanic emissions.

The FLEXPART simulated a priori distribution ($\mu g\,m^{-2}$) of the ash clouds over the eastern Mediterranean at 20:45 UTC, using meteorological fields "w/o" and "w" Aeolus wind assimilation, is shown in Fig. 5a and b. The ash plume is shown to arrive over Antikythera from the west only when Aeolus assimilated wind fields were used (Fig. 5b). In contrast, the volcanic plume in the "w/o" Aeolus forecast never crosses Antikythera, as the forecasted cloud displaced to the north (Fig. 5a).

Additionally, the a posteriori distribution of the ash plume transport ($\mu g\,m^{-2}$) over the eastern Mediterranean at 20:45 UTC, using Aeolus wind assimilation, is shown in Fig. 5c. However, the a posteriori particle emission rates in

the "w/o" Aeolus simulation could not be estimated from the inversion scheme due to very low source–receptor relationships derived from the FLEXPART model (see Appendix A, Fig. A2b, d, and f). As a result, the a posteriori simulation of ash plume transport "w/o" Aeolus assimilation was not produced.

The a posteriori ash plume is notably more concentrated than the a priori plume (Fig. 5b and c) and covers a smaller area, mostly limited to the area around Antikythera and southern Greece. In contrast, the a priori ash plume (Fig. 5b) is more widely dispersed, potentially due to the higher MER values (Fig. 3a, denoted as circles), leading to an overestimation of the a priori ash emissions. The a priori ash plume dispersion extends from the eastern coast of Greece and reaches as far as the western islands. Furthermore, the structure of the a posteriori ash plume closely resembles the ash cloud image captured by the EUMETSAT Meteosat-11 Ash RGB product from the SEVIRI satellite above Antikythera island on 12 March 2021 at 20:45 UTC (Fig. 5d), again highlighting the importance of constraining the variability of the simulation results toward a more stable solution.

A thorough evaluation of the different model simulations is performed against the quality-assured lidar measurements of the PANGEA-NOA observatory. Figure 6 presents the vertical profiles of the FLEXPART simulated ash mass concentrations over PANGEA-NOA. FLEXPART vertical time–height cross-sections of volcanic ash a priori and a posteriori concentration "w" Aeolus assimilated fields (Fig. 6b and c) show a similar pattern to the observed volcanic aerosol layer over Antikythera (Fig. 2a) but reveal significant differences in the vertical distribution and ash mass concentrations.

Specifically, the a priori simulation using "w" Aeolus wind assimilation forecasts a volcanic ash layer at an altitude range of approximately 7.5 to 11 km a.s.l., with ash concentrations reaching below 100 $\mu g\,m^{-3}$ over Antikythera between 18:30 and 21:30 UTC (Fig. 6b). In contrast, the a priori run "w/o" Aeolus assimilation fails to capture the observed ash particle concentrations over Antikythera (Fig. 6a). In the a posteriori simulation, the ash plume driven by the Aeolus wind fields is notably more aligned and better defined than in the a priori simulation with respect to the observed ash plume (Figs. 2 and 6c). The a posteriori profile reveals a volcanic ash layer at an altitude range of 8 to 12 km with higher ash concentrations than in the a priori layer, reaching up to 200 $\mu g\,m^{-3}$ over Antikythera during the same time period (Fig. 6c). Notably, in the a posteriori profile (Fig. 6c), the main part of the ash plume with the highest concentrations is confined between 9 and 11 km, consistent with the observed lidar profile (Fig. 2a). However, the a posteriori FLEXPART time–height cross-sections using the "w/o" Aeolus wind fields were not calculated, as the a posteriori emission rates could not be estimated by the inversion scheme due to very low SRRs derived from the FLEXPART model (see Appendix A, Fig. A2b, d, and f).

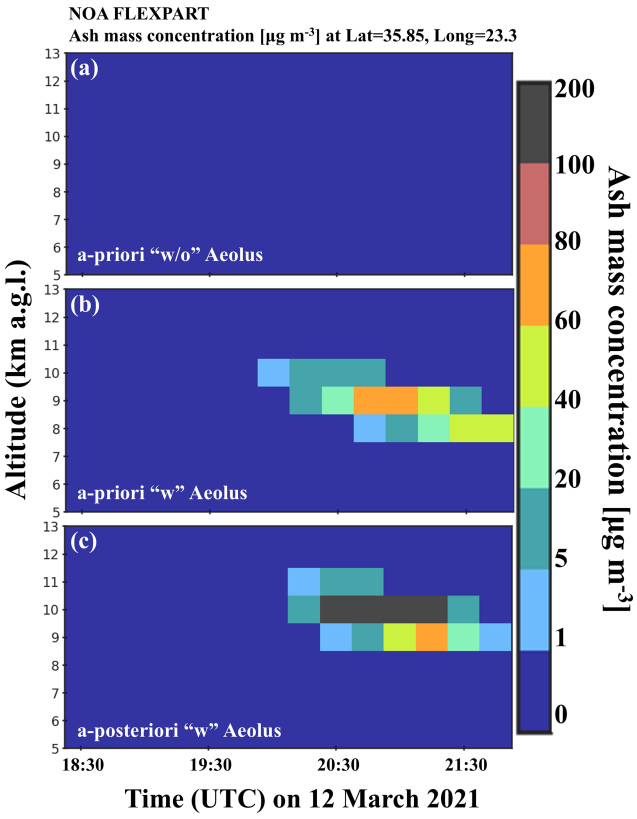

Figure 6. FLEXPART time–height cross-sections on 12 March 2021 at 18:30–21:30 UTC over the PANGEA observatory in Antikythera, Greece. **(a)** Time–height plot of a priori FLEXPART volcanic ash concentrations ($\mu g\,m^{-3}$) "w/o" Aeolus wind assimilation over Antikythera, Greece (zero values). **(b)** Time–height plot of a priori FLEXPART volcanic ash concentrations ($\mu g\,m^{-3}$) "w" Aeolus wind assimilation over Antikythera. **(c)** Time–height plot of a posteriori FLEXPART volcanic ash concentrations ($\mu g\,m^{-3}$) "w" Aeolus wind assimilation over Antikythera, Greece ("w/o" are not calculated). All heights are given in kilometers above ground level.

The better agreement in both the vertical distribution and the concentration of the volcanic ash in the a posteriori simulation (Fig. 6c), compared to the time–height profile of the observed ash plume derived from Polly^{XT} lidar on 12 March from 18:30 to 21:30 UTC (Fig. 2a), highlights the effectiveness of the inversion process when utilizing Aeolus wind data.

The aerosol optical property profiles retrieved from the lidar data are shown in Fig. 7. The POLIPHON method as described in Sect. 3.1.1 was utilized to derive the pure-ash mass concentration profiles.

Polly^{XT} lidar retrievals show that the volcanic ash concentrations over PANGEA-NOA reached up to almost $250 \pm 80\,\mu g\,m^{-3}$ at the plume's center of mass, which is estimated at 10 km a.g.l. (orange line in Fig. 7c and d). The

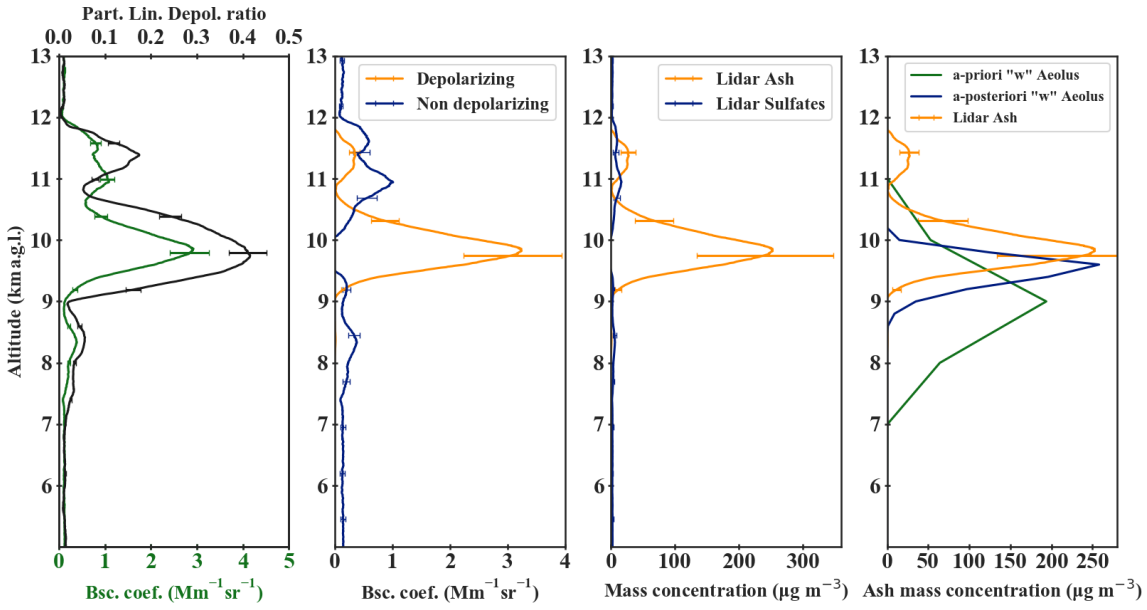

Figure 7. Lidar-derived optical properties over the PANGEA observatory on 12 March 2021 (18:30–21:30 UTC). Vertical distributions of **(a)** total backscatter coefficient (green line) and particle linear depolarization ratio at 532 nm (black line), **(b)** depolarizing (orange line) and non-depolarizing (blue line) particle backscatter coefficient, **(c)** volcanic mass concentrations using the POLIPHON method for ash (orange line) and sulfates (blue line), and **(d)** vertical profile of volcanic ash. Volcanic ash mass concentrations using the POLIPHON method (orange line); FLEXPART a priori model simulations "w" Aeolus assimilated winds (green line), the result of Amiridis et al. (2023) for the fine particles (3, 5, 9, and 21 µm diameter); FLEXPART a posteriori model simulations "w" Aeolus assimilated winds (blue line) for the fine particles (3, 5, 9, and 21 µm diameter); and a priori and a posteriori ash mass concentrations "w/o" Aeolus simulation equal to zero are not shown. All heights are given in kilometers above ground level.

uncertainty in mass concentration calculation is marked with a black error bar in Fig. 7a.

The a posteriori ash emissions from the "w" Aeolus simulation, obtained through the inversion scheme (Fig. 3, stars), were used as input for a new FLEXPART forward run. This run was conducted to estimate a posteriori ash mass concentrations above the PANGEA-NOA station between 18:30 and 21:30 UTC, focusing on fine ash particles with a diameter of 3, 5, 9, and 21 µm.

Figure 7d compares the vertical profiles of the observed and the simulated (a priori and a posteriori "w" Aeolus assimilation) volcanic ash concentrations. The a priori and a posteriori ash mass concentrations "w/o" Aeolus simulation equals zero and are not shown as the SRM derived using "w/o" Aeolus assimilated wind fields results in negligible sensitivities. The volcanic ash plume in the "w/o" Aeolus simulation never reached Antikythera on 12 March 2021 between 18:00 and 21:30 UTC due to a northward shift (Fig. 5a).

The corresponding mass concentrations derived from the FLEXPART a priori simulation (green line) and a posteriori simulation (blue line) are shown in Fig. 7d for comparison with the lidar observations (orange line).

The a priori simulation produced ash concentrations of approximately 150–180 µg m^{-3} at the plume's center of mass, at 8.5 km a.g.l. (green line in Fig. 7d). While the a priori profile shows good spatiotemporal agreement with the lidar retrievals (orange line in Fig. 7d), there is a slight vertical shift of 1 km between the modeled and observed ash mass peaks, which is critical for aviation safety. Furthermore, there is a misfit of about 50 µg m^{-3} between the ash concentrations derived by the Polly^{XT} lidar and those reproduced by the model in the a priori simulation, even with Aeolus data assimilated.

In contrast, when comparing the modeled a posteriori ash mass concentrations to the lidar observations, their agreement is evident when Aeolus winds are assimilated. The maximum ash mass concentration is approximately 250 µg m^{-3} at 9.8 km, closely matching the peak observed by the lidar, while the vertical distribution of the ash plume is also depicted with high accuracy. The difference between the observed and the a posteriori simulated ash mass concentrations is minimal and only 2 %. In contrast, the difference between the lidar observations and the a priori ash simulations ranged from 28 % to 40 %. This demonstrates that the estimated emission profile obtained from the inversion algorithm presented herein is remarkably robust. Overall, the inversion profile yields a much better agreement with lidar observations, confirming the effectiveness of the inversion process and the value of incorporating Aeolus wind data into the model.

5 Conclusions and discussion

The present study presented an inversion method to estimate the volcanic emission rate profile with a Lagrangian particle dispersion model and a ground-based lidar system. The technique was applied to the case study of the explosive eruption of Mt. Etna, Italy, on 12 March 2021. To assess the impact of Aeolus wind assimilation in volcanic ash dispersion forecasts, the simulation was repeated twice: once with Aeolus data assimilated ("w" experiment) and once without ("w/o"). The volcanic aerosol layers observed above the PANGEA-NOA station in Antikythera, along with the clear-sky conditions in the days after the eruption, made this an ideal test case. Important conclusions from our work are as follows:

The Polly^{XT} lidar system of PANGEA-NOA detected a dense aerosol layer between 8 and 12 km, with the volcanic ash plume primarily concentrated between 9 and 11 km. FLEXPART simulations, both a priori (with an empirical emission profile) and a posteriori (with the emission profile produced by the inversion algorithm) were conducted to derive the modeled plume's vertical distribution and concentration. The a priori "w" Aeolus simulation showed a broader dispersion of the ash plume, potentially due to the overestimation of the a priori ash emissions obtained by inverting the observed plume heights from the VONA reports, whereas the a posteriori simulation, based on the inversion results, produced a more refined and consistent ash plume profile, confined to a smaller area, mostly around Antikythera and southern Greece, which was closely similar to the ash cloud observed by the SEVIRI satellite.

In terms of ash mass concentration, the a priori profile with Aeolus wind data assimilated shows a good spatiotemporal agreement with the lidar retrievals but exhibited a slight vertical shift of 1 km with respect to the observed ash mass peaks (Amiridis et al., 2023) along with a misfit in mass concentrations of about 50 $\mu g\,m^{-3}$, a critical factor for aviation safety. In contrast, the a posteriori ash mass concentrations demonstrate a better agreement with the observations above PANGEA-NOA when Aeolus winds are assimilated. The maximum ash mass concentration is found close to 255 $\mu g\,m^{-3}$ at 9.8 km, closely matching the peak observed by the lidar, depicting a minimal difference of the order of 2 % between the observed and the a posteriori simulated ash mass concentrations. In contrast, the difference between the lidar observations and the a priori ash simulations ranged from 28 % to 40 %. This consistency highlights the robustness of the new inversion algorithm and the significant improvement in the vertical distribution and the ash mass concentration. However, additional independent datasets, such as ground-based, satellite remote sensing data, or airborne in situ measurements along the plume's trajectory, would further enhance the validation of this methodology and should be considered in future studies.

To further assess the reliability of the retrieved emissions, a Monte Carlo error propagation analysis was conducted, introducing normally distributed perturbations to the lidar measurements. With this method, the standard deviation of the retrieved emissions at each height level was estimated. The results indicate that the inversion output remained highly stable, with minimal variation across Monte Carlo realizations, suggesting that the single-station observational setup does not introduce significant uncertainty. To enhance the sensitivity of the inversion framework and provide a more comprehensive uncertainty assessment, multiple lidar stations or complementary remote sensing techniques are essential.

The accuracy of the FLEXPART a posteriori simulation is highly dependent on the precision of the driving meteorological fields ("w" Aeolus wind fields), as well as on volcano source parameters such as the plume height and mass eruption rates, which are refined through the inversion process (a posteriori MER).

The advantages of Aeolus wind assimilation for global NWP models have been well documented, particularly by Rennie et al. (2021), who demonstrated significant improvements in wind field representation, especially in the tropics and Southern Hemisphere. Further enhancements in wind forecasts were observed in the study of Amiridis et al. (2023), where regional NWP models benefited from Aeolus wind assimilation. Our case study validates these findings, showing that the assimilation of Aeolus wind profiles leads to a significant improvement in the estimation of volcanic emission rates in the vertical distribution, optimizing the agreement between lidar observations and a posteriori model simulation.

Real-time applications, such as those of VAACs, demand a rapid response to volcanic ash hazards. Once the plume is detected and initial data from lidar systems become available, the presented method can quickly provide the necessary information to calculate the current and future position and extent of the plume within a few hours. This underscores the imperative for high-quality, rapidly accessible data, such as that provided by organized ground-based lidar networks employing standardized algorithms and procedures, such as those used by EARLINET, a key component of the ACTRIS infrastructure.

However, their applicability to the proposed methodology depends on the operation of a backscatter-depolarization lidar, which constitutes the primary requirement. In cases where direct measurements of essential parameters, such as lidar ratios, are unavailable, values from the scientific literature can be used. A more advanced configuration, incorporating Raman lidar capabilities, would enhance the accuracy of retrieved backscatter and lidar ratio coefficients. Additionally, for daytime measurements, a co-located sun photometer would facilitate the direct estimation of the conversion factors required in the inversion process. Beyond ground-based applications, the methodology is also applicable to spaceborne aerosol lidars, which provide vertical profiles of the backscatter coefficient and particle linear depolarization ratio, both fundamental parameters for the inversion process.

Furthermore, the methodology presented herein can be applied to current or future satellite missions that employ lidar measurements (e.g., the EarthCARE mission). While passive satellites offer near-global coverage of ash cloud measurements within minutes to hours, ground-based or satellite lidar systems provide more accurate direct retrievals of the vertical distribution within the ash plume column.

Our methodology is broadly applicable and efficient enough for real-time implementation. It can supply ash forecasting models with an objectively derived quantitative source term, leading to improved forecasts that are critical for the aviation sector. These enhanced forecasts provide more effective emergency responses, ensuring safer and more efficient flight operations during volcanic eruptions, while at the same time minimizing the risk of accidents and the financial impact of flight cancelations.

Appendix A

The SRR for a size distribution of volcanic ash particles with four size bins (3, 5, 9, and 21 µm diameter), derived from the FLEXPART model using the "w" Aeolus assimilated wind fields, indicate that the volcanic emissions observed above the PANGEA-NOA observatory (receptor – y axis) on 12 March 2021 (from 18:30 to 21:30 UTC) at the height range of 6–12 km mostly originate from release heights between 5 and 11.5 km above the Etna volcano (source – x axis) (Fig. A2a, c, and e). These source release heights are consistent with the observed emissions above the PANGEA-NOA station, particularly when the particle release time was 06:00–08:00 and 08:00–10:00 UTC. The source heights for the fine particles align well with the eruptive column heights, as reported from the INGV-OE calibrated cameras (Fig. 1). Additionally, the inversion algorithm was utilized with the FLEXPART SRR only for these two release times. In contrast, the SRR using "w/o" Aeolus assimilated wind fields shows that the volcanic particles arriving above the PANGEA station at heights of 8–10 km (receptor – y axis) are few and originate from release heights of around 8–11 km above Etna (source – x axis) and only when the particle release time was 04:00–06:00 UTC (Fig. A2b, d, and f). This release time is not accurate, as the eruption actually began at 06:00 UTC according to the VONA messages from INGV-EO.

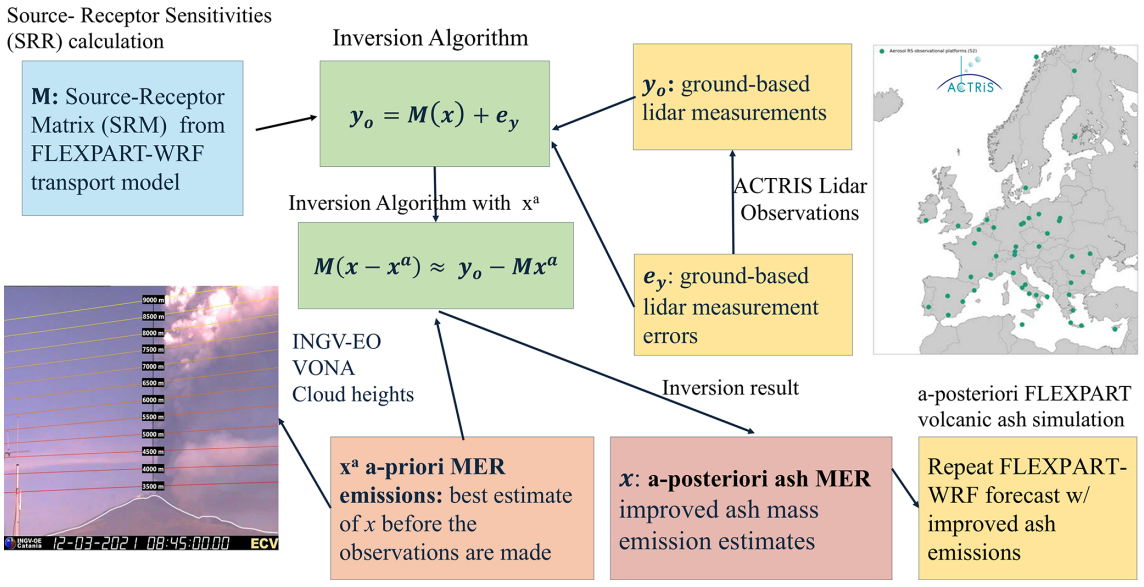

Figure A1. Workflow of the methodology.

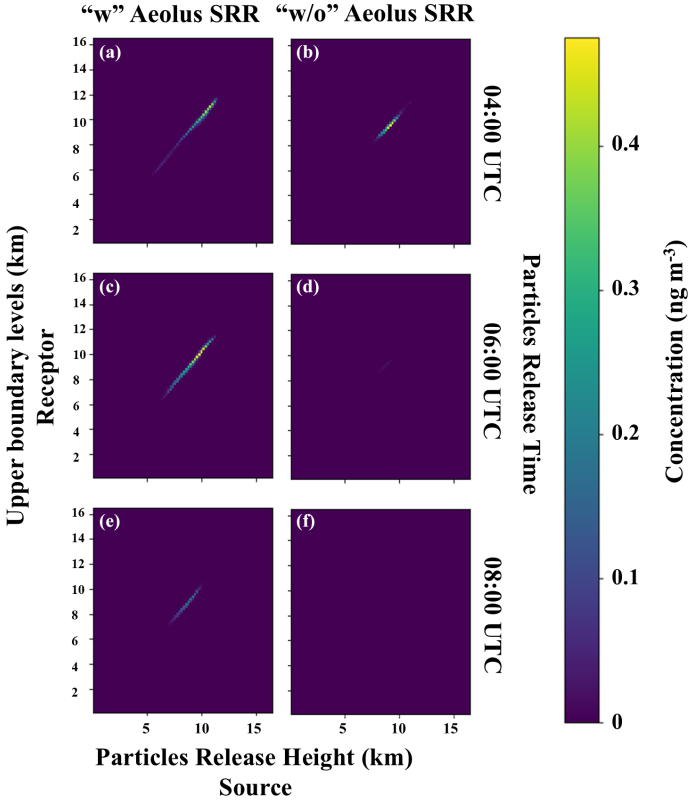

Figure A2. Source–receptor sensitivities for the fine particles (3, 5, 9, and 21 µm diameter) "w" Aeolus assimilated winds (**a**, **c**, and **e**) and "w/o" Aeolus simulation (**b**, **d**, and **f**). The horizontal axis "x" depicts the particle release height (km) above Etna, and the vertical axis "y" is the altitude above PANGEA that the emissions observed on 12 March 2021 (18:30 to 21:30 UTC).

Table A1. Volcanic ash plume heights (m) during the eruption activity from 06:30 to 10:30 UTC, as recorded by the ECV camera operated by INGV-EO (second column) and adjusted heights incorporating SEVIRI satellite observations where applicable (third column).

Time (UTC)	Height (m) from ECV camera (INGV-EO)	Height (m) incorporating SEVIRI observations
06:30	4000	4000
06:45	5500	5500
07:00	5500	5500
07:15	6000	6000
07:30	6500	6500
07:45	7000	7000
08:00	7500	7500
08:15	< 9000	11 500
08:30	< 9000	11 500
08:45	< 9000	11 500
09:00	< 9000	10 000
09:15	< 9000	9500
09:30	< 9000	9500
09:45	9000	9000
10:00	6500	6500
10:15	5000	5000
10:30	4500	4500

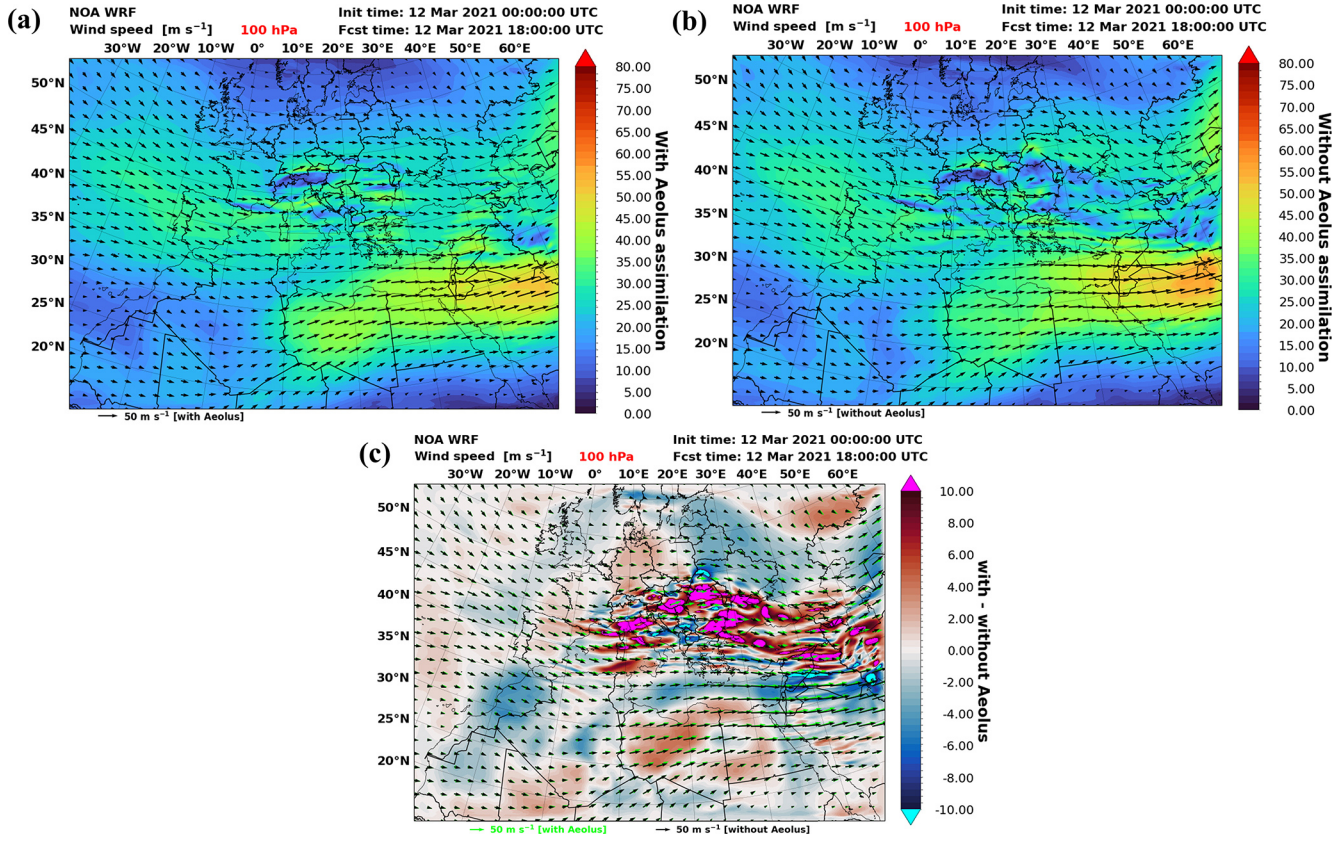

Figure A3. Wind speed ($m s^{-1}$) in WRF 18 h forecasts. Horizontal winds **(a)** "w" Aeolus assimilation, **(b)** "w/o" Aeolus assimilation, and **(c)** wind speed differences ("w" – "w/o" Aeolus assimilation) at 100 hPa (~ 16 km).

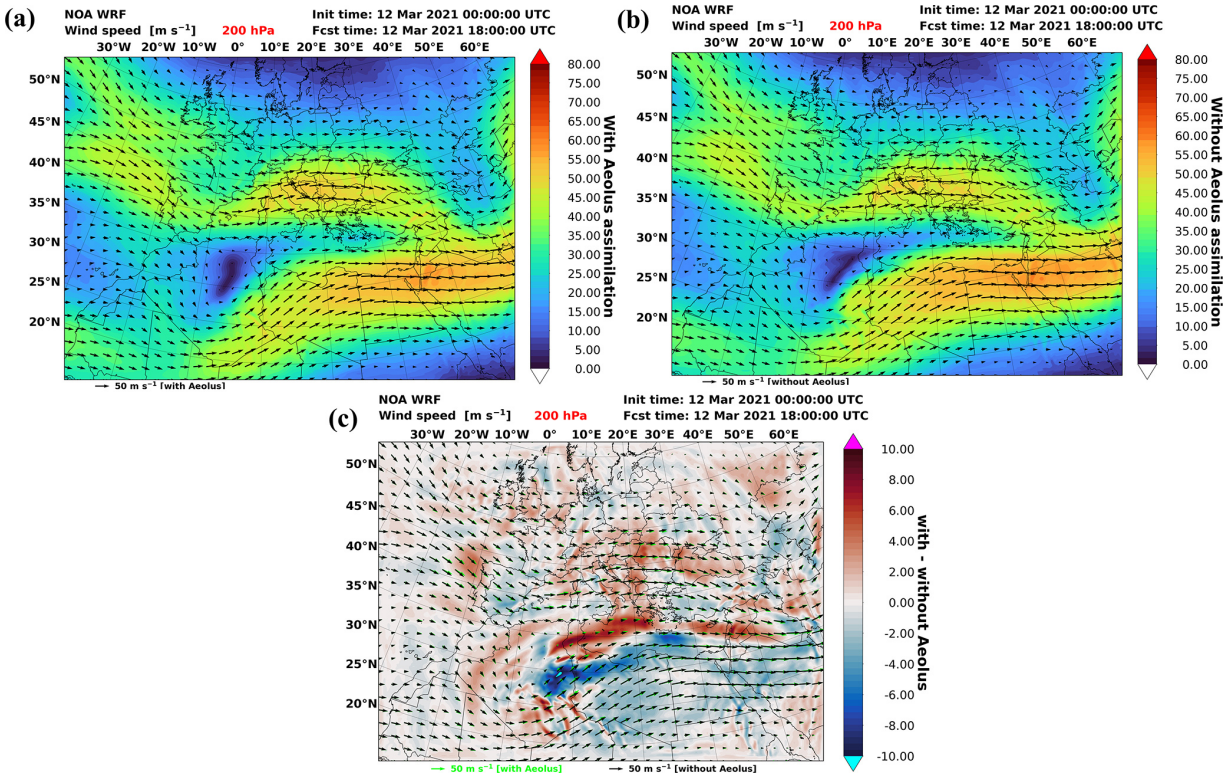

Figure A4. Wind speed ($m\,s^{-1}$) in WRF 18 h forecasts. Horizontal winds **(a)** "w" Aeolus assimilation, **(b)** "w/o" Aeolus assimilation, and **(c)** wind speed differences ("w" – "w/o" Aeolus assimilation) at 200 hPa (~ 12 km).

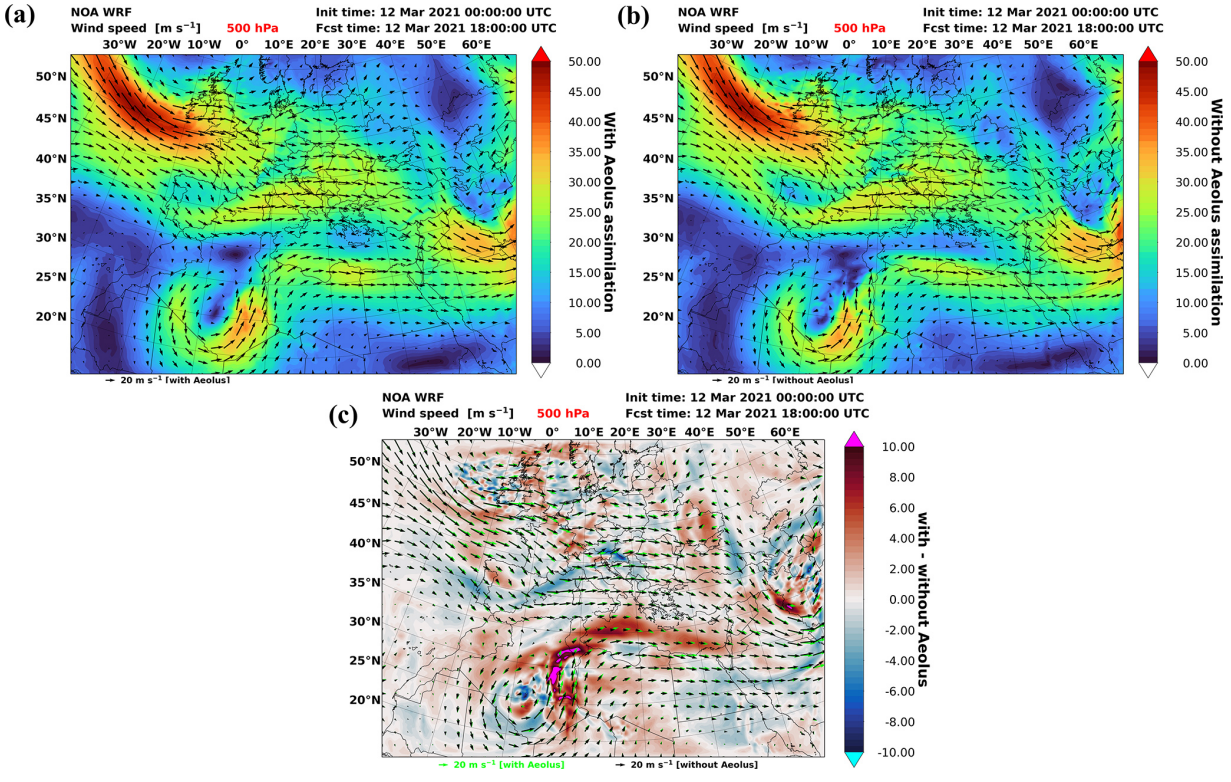

Figure A5. Wind speed ($m\,s^{-1}$) in WRF 18 h forecasts. Horizontal winds **(a)** "w" Aeolus assimilation, **(b)** "w/o" Aeolus assimilation, and **(c)** wind speed differences ("w" – "w/o" Aeolus assimilation) at 500 hPa (~ 5.5 km).

Code availability. The inversion algorithm was written with Python programming language version 3.12 (https://www.python.org/, last access: 27 June 2025) and can be obtained from the co-author Anna Kampouri (akampouri@noa.gr) upon request. The WRF model code is publicly available, has a digital object identifier (https://doi.org/10.5065/D6MK6B4K, UCAR, 2025; Skamarock et al., 2019), and can be obtained via GitHub (https://github.com/wrf-model/WRF, last access: 27 June 2025). The FLEXPART-WRF model code is publicly available and can be obtained from https://git.nilu.no/flexpart/flexpart-wrf (Dingwell, 2025; Brioude et al., 2013) input. The code used for data processing was written with Python programming language version 3.12 (https://www.python.org/, last access: 2 July 2025) and can be obtained via GitHub at https://github.com/NOA-ReACT/Aeolus_Volcano_2023 (last access: 2 July 2025; https://doi.org/10.5281/zenodo.15805552, Kampouri, 2025). The SCC algorithm used here is developed within the EARLINET/ACTRIS community, and its source code is not publicly available. Instead, it is used internally to process raw lidar signals into quality-assured Level 2 optical property profiles, which are made publicly available via the EARLINET data portal (https://data.earlinet.org/, last access: 10 July 2025). The retrievals and the aerosol lidar optical properties are available from the co-author Anna Gialitaki (togialitaki@noa.gr) upon request.

Data availability. The Aeolus L2A wind data can be downloaded from https://apps.ecmwf.int/mars-catalogue/?class=rd&expver=hkv (ECMWF, 2021b, a). The lidar data from the Polly^{XT} system at the PANGEA-NOA station are available in ascii format through Zenodo under the following DOI: https://doi.org/10.5281/zenodo.15805552 (Kampouri, 2025). These data were derived using the Single Calculus Chain (SCC; https://scc.imaa.cnr.it) algorithm (a signal-analysis tool for raw lidar data processing developed within EARLINET (https://www.earlinet.org/, last access: 3 July 2025) and ACTRIS (https://www.actris.eu/, last access: 3 July 2025)). SCC products (L2 optical property profiles) are publicly available through the EARLINET data portal (https://github.com/actris-ares/actris-earlinet-2024_annual_collection/tree/main, ACTRIS EARLINET, 2024). The WRF and FLEXPART-WRF models' simulation results are also available from the co-author Anna Kampouri (akampouri@noa.gr) upon request.

Author contributions. AK conceptualized the paper along with VA, PZ, and StS. All authors wrote parts of the paper corresponding to their work and respective results. AK performed the FLEXPART and WRF runs and the inversion algorithm with the support of StS, PZ, and TG. AG and MT provided the Polly^{XT} lidar retrievals. SiS provided the INGV-OE camera material and synergistic datasets for the analysis. MR provided the ECMWF-IFS datasets ("w" and "w/o" Aeolus assimilation). All authors provided corrections and suggestions to eventually shape the research, analysis, and final paper. AK supervised and directed the whole project.

Competing interests. The contact author has declared that none of the authors has any competing interests.

Disclaimer. Publisher's note: Copernicus Publications remains neutral with regard to jurisdictional claims made in the text, published maps, institutional affiliations, or any other geographical representation in this paper. While Copernicus Publications makes every effort to include appropriate place names, the final responsibility lies with the authors.

Acknowledgements. Anna Kampouri and the authors affiliated to the National Observatory of Athens acknowledge the support from the following research projects: the PANORAMA project, funded by the European Union (grant agreement 101182795); the PANGEA4CalVal project, funded by the European Union (grant agreement 101079201); the Hellenic Foundation for Research and Innovation (project abbreviation: StratoFIRE, project number: 3995); the e-shape project, under the European Union's Horizon 2020 research and innovation program (grant agreement 820852); the ACTRIS research infrastructure; and data and services obtained from the PANhellenic GEophysical Observatory of Antikythera (PANGEA) of NOA. Additionally, Anna Kampouri and Thanasis Georgiou acknowledge support from ESA in the framework of the "Enhancing Aeolus L2A for depolarizing targets and impact on aerosol research and NWP" project (4000139424/22/I-NS). Anna Kampouri acknowledges the support from Ioanni Binietoglou, Antoni Gkika, and Emmanouil Proestaki for their invaluable assistance and insightful discussions throughout the development of this work. Additionally, the authors thank the two anonymous reviewers for their helpful comments and suggestions for improving the quality of the paper.

Financial support. This research has been supported by the Hellenic Foundation for Research and Innovation (Project Acronym: StratoFIRE, grant no. 3995).

Review statement. This paper was edited by Stelios Kazadzis and reviewed by two anonymous referees.

References

ACTRIS: Polly^{XT} lidar data at PANGEA station, National Observatory of Athens [data set], https://polly.tropos.de/calendar/location/38, last access: 3 July 2025.

ACTRIS EARLINET: ACTRIS EARLINET 2024 Annual Collection – Antikythera (AKY): Aerosol Optical and Microphysical Properties, CNR-IMAA ARES Data Center [data set], https://github.com/actris-ares/actris-earlinet-2024_annual_collection/tree/main, (last access: 11 July 2025), 2024.

Amiridis, V., Kampouri, A., Gkikas, A., Misios, S., Gialitaki, A., Marinou, E., Rennie, M., Benedetti, A., Solomos, S., Zanis, P., Vasardani, O., Eleftheratos, K., Paschou, P., Georgiou, T., Scollo, S., Mona, L., Papagiannopoulos, N., Retscher, C., Parrinello, T., and Straume, A. G.: Aeolus winds impact on volcanic ash early warning systems for aviation, Sci. Rep.-UK, 13, 7531, https://doi.org/10.1038/s41598-023-34715-6, 2023.

Ansmann, A., Tesche, M., Seifert, P., Groß, S., Freudenthaler, V., Apituley, A., Wilson, K. M., Serikov, I., Linné, H.,

Heinold, B., Hiebsch, A., Schnell, F., Schmidt, J., Mattis, I., Wandinger, U., and Wiegner, M.: Ash and fine-mode particle mass profiles from EARLINET-AERONET observations over central Europe after the eruptions of the Eyjafjallajökull volcano in 2010, J. Geophys. Res.-Atmos., 116, D00U02, https://doi.org/10.1029/2010JD015567, 2011a.

Ansmann, A., Petzold, A., Kandler, K., Tegen, I., Wendisch, M., Müller, D., Weinzierl, B., Müller, T., and Heintzenberg, J.: Saharan Mineral Dust Experiments SAMUM–1 and SAMUM–2: what have we learned?, Tellus B, 63, 403, https://doi.org/10.1111/j.1600-0889.2011.00555.x, 2011b.

Ansmann, A., Seifert, P., Tesche, M., and Wandinger, U.: Profiling of fine and coarse particle mass: case studies of Saharan dust and Eyjafjallajökull/Grimsvötn volcanic plumes, Atmos. Chem. Phys., 12, 9399–9415, https://doi.org/10.5194/acp-12-9399-2012, 2012.

Baars, H., Seifert, P., Engelmann, R., and Wandinger, U.: Target categorization of aerosol and clouds by continuous multiwavelength-polarization lidar measurements, Atmos. Meas. Tech., 10, 3175–3201, https://doi.org/10.5194/amt-10-3175-2017, 2017.

Beckett, F., Rossi, E., Devenish, B., Witham, C., and Bonadonna, C.: Modelling the size distribution of aggregated volcanic ash and implications for operational atmospheric dispersion modelling, Atmos. Chem. Phys., 22, 3409–3431, https://doi.org/10.5194/acp-22-3409-2022, 2022.

Brioude, J., Arnold, D., Stohl, A., Cassiani, M., Morton, D., Seibert, P., Angevine, W., Evan, S., Dingwell, A., Fast, J. D., Easter, R. C., Pisso, I., Burkhart, J., and Wotawa, G.: The Lagrangian particle dispersion model FLEXPART-WRF version 3.1, Geosci. Model Dev., 6, 1889–1904, https://doi.org/10.5194/gmd-6-1889-2013, 2013.

Calvari, S., Bonaccorso, A., and Ganci, G.: Anatomy of a Paroxysmal Lava Fountain at Etna Volcano: The Case of the 12 March 2021, Episode, Remote Sens.-Basel, 13, 3052, https://doi.org/10.3390/rs13153052, 2021.

Chen, F. and Dudhia, J.: Coupling and advanced land surface-hydrology model with the Penn State-NCAR MM5 modeling system. Part I: Model implementation and sensitivity, Mon. Weather Rev., 129, 569–585, 2001.

Clarisse, L., Prata, F., Lacour, J., Hurtmans, D., Clerbaux, C., and Coheur, P.: A correlation method for volcanic ash detection using hyperspectral infrared measurements, Geophys. Res. Lett., 37, 2010GL044828, https://doi.org/10.1029/2010GL044828, 2010.

Clarkson, R. and Simpson, H.: Maximising airspace use during volcanic eruptions: matching engine durability against ash cloud occurrence, in: NATO STO Specialists' Meeting on Impact of Volcanic Ash Clouds on Military Operations (STO-MP-AVT-272), Melbourne, Australia, 16–18 May 2017, NATO Science and Technology Organization, 15–17, https://www.researchgate.net/publication/317617735_Maximising_Airspace_Use_During_Volcanic_Eruptions_Matching_Engine_Durability_against_Ash_Cloud_Occurrence (last access: 10 July 2025), 2017.

Corradini, S., Guerrieri, L., Lombardo, V., Merucci, L., Musacchio, M., Prestifilippo, M., Scollo, S., Silvestri, M., Spata, G., and Stelitano, D.: Proximal Monitoring of the 2011–2015 Etna Lava Fountains Using MSG-SEVIRI Data, Geosciences, 8, 140, https://doi.org/10.3390/geosciences8040140, 2018.

Dacre, H. F., Grant, A. L. M., Hogan, R. J., Belcher, S. E., Thomson, D. J., Devenish, B. J., Marenco, F., Hort, M. C., Haywood, J. M., Ansmann, A., Mattis, I., and Clarisse, L.: Evaluating the structure and magnitude of the ash plume during the initial phase of the 2010 Eyjafjallajökull eruption using lidar observations and NAME simulations, J. Geophys. Res., 116, D00U03, https://doi.org/10.1029/2011JD015608, 2011.

D'Amico, G., Amodeo, A., Baars, H., Binietoglou, I., Freudenthaler, V., Mattis, I., Wandinger, U., and Pappalardo, G.: EARLINET Single Calculus Chain – overview on methodology and strategy, Atmos. Meas. Tech., 8, 4891–4916, https://doi.org/10.5194/amt-8-4891-2015, 2015.

Degruyter, W. and Bonadonna, C.: Improving on mass flow rate estimates of volcanic eruptions, Geophys. Res. Lett., 39, 2012GL052566, https://doi.org/10.1029/2012GL052566, 2012.

Dingwell, A.: FLEXPART-WRF code, NILU GitLab repository [code], https://git.nilu.no/flexpart/flexpart-wrf, last access: 10 July 2025.

Dubovik, O., Sinyuk, A., Lapyonok, T., Holben, B. N., Mishchenko, M., Yang, P., Eck, T. F., Volten, H., Muñoz, O., Veihelmann, B., Van Der Zande, W. J., Leon, J., Sorokin, M., and Slutsker, I.: Application of spheroid models to account for aerosol particle nonsphericity in remote sensing of desert dust, J. Geophys. Res., 111, 2005JD006619, https://doi.org/10.1029/2005JD006619, 2006.

Durant, A. J., Bonadonna, C., and Horwell, C. J.: Atmospheric and Environmental Impacts of Volcanic Particulates, Elements, 6, 235–240, https://doi.org/10.2113/gselements.6.4.235, 2010.

Eckhardt, S., Prata, A. J., Seibert, P., Stebel, K., and Stohl, A.: Estimation of the vertical profile of sulfur dioxide injection into the atmosphere by a volcanic eruption using satellite column measurements and inverse transport modeling, Atmos. Chem. Phys., 8, 3881–3897, https://doi.org/10.5194/acp-8-3881-2008, 2008.

ECMWF: Synoptic-scale variability in the Mediterranean, ECMWF Technical Report No. 60, European Centre for Medium-Range Weather Forecasts, Reading, UK, https://www.ecmwf.int/en/elibrary/78648-synoptic-scale-variability-mediterranean (last access: 9 July 2025), 2010.

ECMWF: ECMWF starts assimilating Aeolus wind data, European Centre for Medium-Range Weather Forecasts, Reading, UK, https://www.ecmwf.int/en/about/media-centre/news/2020/ecmwf-starts-assimilating-aeolus-wind-data (last access: 9 July 2025), 2021a.

ECMWF: Aeolus L2A wind data, European Centre for Medium-Range Weather Forecasts [data set], https://apps.ecmwf.int/mars-catalogue/?class=rd&expver=hkv (last access: 3 July 2025), 2021b.

Engelmann, R., Kanitz, T., Baars, H., Heese, B., Althausen, D., Skupin, A., Wandinger, U., Komppula, M., Stachlewska, I. S., Amiridis, V., Marinou, E., Mattis, I., Linné, H., and Ansmann, A.: The automated multiwavelength Raman polarization and water-vapor lidar Polly^{XT}: the neXT generation, Atmos. Meas. Tech., 9, 1767–1784, https://doi.org/10.5194/amt-9-1767-2016, 2016.

EUROCONTROL: Forecast Update 2022–2028, European Flight Movements and Service Units, EUROCONTROL, Brussels, Belgium, https://www.eurocontrol.int/publication/eurocontrol-forecast-update-2022-2028 (last access: 9 July 2025), 2022.

Fang, S., Dong, X., Zhuang, S., Tian, Z., Chai, T., Xu, Y., Zhao, Y., Sheng, L., Ye, X., and Xiong, W.: Oscillation-free source term inversion of atmospheric radionuclide releases with joint model bias corrections and non-smooth competing priors, J. Hazard. Mater., 440, 129806, https://doi.org/10.1016/j.jhazmat.2022.129806, 2022.

Fearnley, C. J., Bird, D. K., Haynes, K., McGuire, W. J., and Jolly, G. (Eds.): Observing the Volcano World: Volcano Crisis Communication, Springer International Publishing, Cham, https://doi.org/10.1007/978-3-319-44097-2, 2018.

Floutsi, A. A., Baars, H., Engelmann, R., Althausen, D., Ansmann, A., Bohlmann, S., Heese, B., Hofer, J., Kanitz, T., Haarig, M., Ohneiser, K., Radenz, M., Seifert, P., Skupin, A., Yin, Z., Abdullaev, S. F., Komppula, M., Filioglou, M., Giannakaki, E., Stachlewska, I. S., Janicka, L., Bortoli, D., Marinou, E., Amiridis, V., Gialitaki, A., Mamouri, R.-E., Barja, B., and Wandinger, U.: DeLiAn – a growing collection of depolarization ratio, lidar ratio and Ångström exponent for different aerosol types and mixtures from ground-based lidar observations, Atmos. Meas. Tech., 16, 2353–2379, https://doi.org/10.5194/amt-16-2353-2023, 2023.

Francis, P. N., Cooke, M. C., and Saunders, R. W.: Retrieval of physical properties of volcanic ash using Meteosat: A case study from the 2010 Eyjafjallajökull eruption, J. Geophys. Res., 117, 2011JD016788, https://doi.org/10.1029/2011JD016788, 2012.

Gasteiger, J., Groß, S., Freudenthaler, V., and Wiegner, M.: Volcanic ash from Iceland over Munich: mass concentration retrieved from ground-based remote sensing measurements, Atmos. Chem. Phys., 11, 2209–2223, https://doi.org/10.5194/acp-11-2209-2011, 2011.

Giannakaki, E., Pfüller, A., Korhonen, K., Mielonen, T., Laakso, L., Vakkari, V., Baars, H., Engelmann, R., Beukes, J. P., Van Zyl, P. G., Josipovic, M., Tiitta, P., Chiloane, K., Piketh, S., Lihavainen, H., Lehtinen, K. E. J., and Komppula, M.: One year of Raman lidar observations of free-tropospheric aerosol layers over South Africa, Atmos. Chem. Phys., 15, 5429–5442, https://doi.org/10.5194/acp-15-5429-2015, 2015.

Giles, D. M., Sinyuk, A., Sorokin, M. G., Schafer, J. S., Smirnov, A., Slutsker, I., Eck, T. F., Holben, B. N., Lewis, J. R., Campbell, J. R., Welton, E. J., Korkin, S. V., and Lyapustin, A. I.: Advancements in the Aerosol Robotic Network (AERONET) Version 3 database – automated near-real-time quality control algorithm with improved cloud screening for Sun photometer aerosol optical depth (AOD) measurements, Atmos. Meas. Tech., 12, 169–209, https://doi.org/10.5194/amt-12-169-2019, 2019.

Goloub, P., Li, Z., Dubovik, O., Blarel, L., Podvin, T., Jankowiak, I., Lecoq, R., Deroo, C., Chatenet, B., Morel, J. P., Cuevas, E., and Ramos, R.: PHOTONS/AERONET sunphotometer network overview: description, activities, results, SPIE Proc., 69360V-69360V–15, https://doi.org/10.1117/12.783171, 2007.

Groß, S., Freudenthaler, V., Wiegner, M., Gasteiger, J., Geiß, A., and Schnell, F.: Dual-wavelength linear depolarization ratio of volcanic aerosols: Lidar measurements of the Eyjafjallajökull plume over Maisach, Germany, Atmos. Environ., 48, 85–96, https://doi.org/10.1016/j.atmosenv.2011.06.017, 2012.

Groß, S., Esselborn, M., Weinzierl, B., Wirth, M., Fix, A., and Petzold, A.: Aerosol classification by airborne high spectral resolution lidar observations, Atmos. Chem. Phys., 13, 2487–2505, https://doi.org/10.5194/acp-13-2487-2013, 2013.

Guerrieri, L., Corradini, S., Theys, N., Stelitano, D., and Merucci, L.: Volcanic Clouds Characterization of the 2020–2022 Sequence of Mt. Etna Lava Fountains Using MSG-SEVIRI and Products' Cross-Comparison, Remote Sens.-Basel, 15, 2055, https://doi.org/10.3390/rs15082055, 2023.

Guffanti, M., Ewert, J. W., Gallina, G. M., Bluth, G. J. S., and Swanson, G. L.: Volcanic-ash hazard to aviation during the 2003–2004 eruptive activity of Anatahan volcano, Commonwealth of the Northern Mariana Islands, J. Volcanol. Geoth. Res., 146, 241–255, https://doi.org/10.1016/j.jvolgeores.2004.12.011, 2005.

Harvey, N. J., Dacre, H. F., Webster, H. N., Taylor, I. A., Khanal, S., Grainger, R. G., and Cooke, M. C.: The Impact of Ensemble Meteorology on Inverse Modeling Estimates of Volcano Emissions and Ash Dispersion Forecasts: Grímsvötn 2011, Atmosphere, 11, 1022, https://doi.org/10.3390/atmos11101022, 2020.

Hess, M., Koepke, P., and Schult, I.: Optical Properties of Aerosols and Clouds: The Software Package OPAC, B. Am. Meteorol. Soc., 79, 831–844, https://doi.org/10.1175/1520-0477(1998)079<0831:OPOAAC>2.0.CO;2, 1998.

Houchi, K., Stoffelen, A., Marseille, G. J., and De Kloe, J.: Comparison of wind and wind shear climatologies derived from high-resolution radiosondes and the ECMWF model, J. Geophys. Res., 115, 2009JD013196, https://doi.org/10.1029/2009JD013196, 2010.

Iacono, M. J., Delamere, J. S, Mlawer, E. J, Shephard, M. W., Clough, S. A, and Collins, W. D.: Radiative forcing by long-lived greenhouse gases: Calculations with the AER radiative transfer models, J. Geophys. Res.-Atmos., 113, D13103, https://doi.org/10.1029/2008JD009944, 2008.

ICAO: North Atlantic Systems Planning Group – Fifty-second meeting report (NAT SPG/52), 20–24 June 2016, Paris, France, European and North Atlantic (EUR/NAT) Office, International Civil Aviation Organization, Montreal, Canada, https://www.icao.int/EURNAT/EUR%20and%20NAT%20Documents/NAT%20Documents/NAT%20SPG%20Reports/NAT%20SPG_52%20(2016)%20Report.pdf (last access: 9 July 2025), 2016.

INGV: Osservatorio Etneo, Istituto Nazionale di Geofisica e Vulcanologia (INGV), https://www.ct.ingv.it/, last access: 2 July 2025.

Janjic, Z. I.: Nonsingular implementation of the Mellor-Yamada level 2.5 scheme in the NCEP Meso model, NCEP Office Note 437, National Centers for Environmental Prediction (NCEP), Camp Springs,61 pp., https://repository.library.noaa.gov/view/noaa/11409 (last access: 3 July 2025), 2002.

Janjic, Z. I.: A nonhydrostatic model based on a new approach, Meteorol. Atmos. Phys., 82, 271–285, https://doi.org/10.1007/s00703-001-0587-6, 2003.

Jones, A., Thomson, D., Hort, M., and Devenish, B.: The U. K. Met Office's Next-Generation Atmospheric Dispersion Model, NAME III, in: Air Pollution Modeling and Its Application XVII, Boston, MA, 580–589, https://doi.org/10.1007/978-0-387-68854-1_62, 2007.

Kampouri, A.: akampouri/Volcanic-emission-estimates_Kampouri_et_al.2025: Volcanic emission estimates from the inversion of ACTRIS lidar observations and their use for quantitative dispersion modeling (v1.0.0), Zenodo [code and data set], https://doi.org/10.5281/zenodo.15805552, 2025.

Kampouri, A., Amiridis, V., Solomos, S., Gialitaki, A., Marinou, E., Spyrou, C., Georgoulias, A. K., Akritidis, D., Papagiannopoulos, N., Mona, L., Scollo, S., Tsichla, M., Tsikoudi, I., Pytharoulis, I., Karacostas, T., and Zanis, P.: Investigation of Volcanic Emissions in the Mediterranean: "The Etna–Antikythera Connection", Atmosphere, 12, 40, https://doi.org/10.3390/atmos12010040, 2020.

Kampouri, A., Amiridis, V., Georgiou, T., Solomos, S., Binietoglou, I., Gialitaki, A., Marinou, E., Gkikas, A., Proestakis, E., Rennie, M., Benedetti, A., Scollo, S., Mona, L., Papagiannopoulos, N., and Zanis, P.: Inversion Techniques on Etna's Volcanic Emissions and the Impact of Aeolus on Quantitative Dispersion Modeling, in: 16th International Conference on Meteorology, Climatology and Atmospheric Physics – COMECAP 2023, International Conference on Meteorology, Climatology and Atmospheric Physics, 12–16 June 2023, Thessaloniki, Greece, 187, https://doi.org/10.3390/environsciproc2023026187, 2023.

Koepke, P., Gasteiger, J., and Hess, M.: Technical Note: Optical properties of desert aerosol with non-spherical mineral particles: data incorporated to OPAC, Atmos. Chem. Phys., 15, 5947–5956, https://doi.org/10.5194/acp-15-5947-2015, 2015.

Konsta, D., Tsekeri, A., Solomos, S., Siomos, N., Gialitaki, A., Tetoni, E., Lopatin, A., Goloub, P., Dubovik, O., Amiridis, V., and Nastos, P.: The Potential of GRASP/GARRLiC Retrievals for Dust Aerosol Model Evaluation: Case Study during the PreTECT Campaign, Remote Sens.-Basel, 13, 873, https://doi.org/10.3390/rs13050873, 2021.

Kristiansen, N. I., Stohl, A., Prata, A. J., Richter, A., Eckhardt, S., Seibert, P., Hoffmann, A., Ritter, C., Bitar, L., Duck, T. J., and Stebel, K.: Remote sensing and inverse transport modeling of the Kasatochi eruption sulfur dioxide cloud, J. Geophys. Res., 115, 2009JD013286, https://doi.org/10.1029/2009JD013286, 2010.

Kristiansen, N. I., Stohl, A., Prata, A. J., Bukowiecki, N., Dacre, H., Eckhardt, S., Henne, S., Hort, M. C., Johnson, B. T., Marenco, F., Neininger, B., Reitebuch, O., Seibert, P., Thomson, D. J., Webster, H. N., and Weinzierl, B.: Performance assessment of a volcanic ash transport model mini-ensemble used for inverse modeling of the 2010 Eyjafjallajökull eruption, J. Geophys. Res., 117, 2011JD016844, https://doi.org/10.1029/2011JD016844, 2012.

Kristiansen, N. I., Arnold, D., and Stohl, A.: Procedures for volcano inversions using FLEXPART, Norwegian Institute for Air Research (NILU) VAST Report, Kjeller, Norway, https://nilu.com/wp-content/uploads/dnn/KST-VAST_final_report.pdf (last access: 3 July 2025), 2014.

Lensky, I. M., Dayan, U., and Helman, D.: Synoptic Circulation Impact on the Near-Surface Temperature Difference Outweighs That of the Seasonal Signal in the Eastern Mediterranean, J. Geophys. Res.-Atmos., 123, 11,333-11,347, https://doi.org/10.1029/2017JD027973, 2018.

Li, X., Li, H., Liu, Y., Xiong, W., and Fang, S.: Joint release rate estimation and measurement-by-measurement model correction for atmospheric radionuclide emission in nuclear accidents: An application to wind tunnel experiments, J. Hazard. Mater., 345, 48–62, https://doi.org/10.1016/j.jhazmat.2017.09.051, 2018.

Lopatin, A., Dubovik, O., Chaikovsky, A., Goloub, P., Lapyonok, T., Tanré, D., and Litvinov, P.: Enhancement of aerosol characterization using synergy of lidar and sun-photometer coincident observations: the GARRLiC algorithm, Atmos. Meas. Tech., 6, 2065–2088, https://doi.org/10.5194/amt-6-2065-2013, 2013.

Lopatin, A., Dubovik, O., Fuertes, D., Stenchikov, G., Lapyonok, T., Veselovskii, I., Wienhold, F. G., Shevchenko, I., Hu, Q., and Parajuli, S.: Synergy processing of diverse ground-based remote sensing and in situ data using the GRASP algorithm: applications to radiometer, lidar and radiosonde observations, Atmos. Meas. Tech., 14, 2575–2614, https://doi.org/10.5194/amt-14-2575-2021, 2021.

Mamouri, R.-E. and Ansmann, A.: Potential of polarization/Raman lidar to separate fine dust, coarse dust, maritime, and anthropogenic aerosol profiles, Atmos. Meas. Tech., 10, 3403–3427, https://doi.org/10.5194/amt-10-3403-2017, 2017.

Mastin, L. G., Guffanti, M., Servranckx, R., Webley, P., Barsotti, S., Dean, K., Durant, A., Ewert, J. W., Neri, A., Rose, W. I., Schneider, D., Siebert, L., Stunder, B., Swanson, G., Tupper, A., Volentik, A., and Waythomas, C. F.: A multidisciplinary effort to assign realistic source parameters to models of volcanic ash-cloud transport and dispersion during eruptions, J. Volcanol. Geoth. Res., 186, 10–21, https://doi.org/10.1016/j.jvolgeores.2009.01.008, 2009.

Mazzocchi, M., Hansstein, F., and Ragona, M.: The 2010 volcanic ash cloud and its financial impact on the European airline industry, CESifo Forum, 11, 92–100, https://hdl.handle.net/10419/166397 (last access: 9 July 2025), 2010.

Müller, D., Ansmann, A., Mattis, I., Tesche, M., Wandinger, U., Althausen, D., and Pisani, G.: Aerosol-type-dependent lidar ratios observed with Raman lidar, J. Geophys. Res.-Atmos., 112, D16202, https://doi.org/10.1029/2006JD008292, 2007.

Näslund, E. and Thaning, L.: On the Settling Velocity in a Nonstationary Atmosphere, Aerosol Sci. Tech., 14, 247–256, https://doi.org/10.1080/02786829108959487, 1991.

Oxford Economics: The economic impacts of air travel restrictions due to volcanic ash, prepared for Airbus, Oxford Economics Ltd, Oxford, UK, https://controverses.minesparis.psl.eu/public/promo10/promo10_G11/data/documents/Volcanic-Update.pdf (last access: 3 July 2025), 2012.

Pappalardo, G., Amodeo, A., Mona, L., Pandolfi, M., Pergola, N., and Cuomo, V.: Raman lidar observations of aerosol emitted during the 2002 Etna eruption, Geophys. Res. Lett., 31, 2003GL019073, https://doi.org/10.1029/2003GL019073, 2004.

Pavolonis, M. J., Heidinger, A. K., and Sieglaff, J.: Automated retrievals of volcanic ash and dust cloud properties from upwelling infrared measurements, J. Geophys. Res.-Atmos., 118, 1436–1458, https://doi.org/10.1002/jgrd.50173, 2013.

Petersen, G. N., Bjornsson, H., Arason, P., and von Löwis, S.: Two weather radar time series of the altitude of the volcanic plume during the May 2011 eruption of Grímsvötn, Iceland, Earth Syst. Sci. Data, 4, 121–127, https://doi.org/10.5194/essd-4-121-2012, 2012.

Pisso, I., Sollum, E., Grythe, H., Kristiansen, N. I., Cassiani, M., Eckhardt, S., Arnold, D., Morton, D., Thompson, R. L., Groot Zwaaftink, C. D., Evangeliou, N., Sodemann, H., Haimberger, L., Henne, S., Brunner, D., Burkhart, J. F., Fouilloux, A., Brioude, J., Philipp, A., Seibert, P., and Stohl, A.: The Lagrangian particle dispersion model FLEXPART version 10.4, Geosci. Model Dev., 12, 4955–4997, https://doi.org/10.5194/gmd-12-4955-2019, 2019.

Pouget, S., Bursik, M., Webley, P., Dehn, J., and Pavolonis, M.: Estimation of eruption source parameters from umbrella cloud or downwind plume growth rate, J. Volcanol. Geoth. Res.,

258, 100–112, https://doi.org/10.1016/j.jvolgeores.2013.04.002, 2013.

Prata, A. J.: Satellite detection of hazardous volcanic clouds and the risk to global air traffic, Nat. Hazards, 51, 303–324, https://doi.org/10.1007/s11069-008-9273-z, 2009.

Prata, A. J. and Prata, A. T.: Eyjafjallajökull volcanic ash concentrations determined using Spin Enhanced Visible and Infrared Imager measurements, J. Geophys. Res., 117, 2011JD016800, https://doi.org/10.1029/2011JD016800, 2012.

Prata, A. T., Grainger, R. G., Taylor, I. A., Povey, A. C., Proud, S. R., and Poulsen, C. A.: Uncertainty-bounded estimates of ash cloud properties using the ORAC algorithm: application to the 2019 Raikoke eruption, Atmos. Meas. Tech., 15, 5985–6010, https://doi.org/10.5194/amt-15-5985-2022, 2022.

Prata, F. and Lynch, M.: Passive Earth Observations of Volcanic Clouds in the Atmosphere, Atmosphere, 10, 199, https://doi.org/10.3390/atmos10040199, 2019.

Rennie, M. P., Isaksen, L., Weiler, F., De Kloe, J., Kanitz, T., and Reitebuch, O.: The impact of Aeolus wind retrievals on ECMWF global weather forecasts, Q. J. Roy. Meteor. Soc., 147, 3555–3586, https://doi.org/10.1002/qj.4142, 2021.

Robock, A.: Volcanic eruptions and climate, Rev. Geophys., 38, 191–219, https://doi.org/10.1029/1998RG000054, 2000.

Rousi, E., Mimis, A., Stamou, M., and Anagnostopoulou, C.: Classification of circulation types over Eastern mediterranean using a self-organizing map approach, J. Maps, 10, 232–237, https://doi.org/10.1080/17445647.2013.862747, 2014.

Scollo, S., Coltelli, M., Bonadonna, C., and Del Carlo, P.: Tephra hazard assessment at Mt. Etna (Italy), Nat. Hazards Earth Syst. Sci., 13, 3221–3233, https://doi.org/10.5194/nhess-13-3221-2013, 2013.

Scollo, S., Prestifilippo, M., Pecora, E., Corradini, S., Merucci, L., Spata, G., and Coltelli, M.: Eruption column height estimation of the 2011–2013 Etna lava fountains, Ann. Geophys., 57, 3, https://doi.org/10.4401/ag-6396, 2014.

Scollo, S., Prestifilippo, M., Bonadonna, C., Cioni, R., Corradini, S., Degruyter, W., Rossi, E., Silvestri, M., Biale, E., Carparelli, G., Cassisi, C., Merucci, L., Musacchio, M., and Pecora, E.: Near-Real-Time Tephra Fallout Assessment at Mt. Etna, Italy, Remote Sens.-Basel, 11, 2987, https://doi.org/10.3390/rs11242987, 2019.

Seibert, P. and Frank, A.: Source-receptor matrix calculation with a Lagrangian particle dispersion model in backward mode, Atmos. Chem. Phys., 4, 51–63, https://doi.org/10.5194/acp-4-51-2004, 2004.

Seibert, P., Kristiansen, N. I., Richter, A., Eckhardt, S., Prata, A. J., and Stohl, A.: Uncertainties in the inverse modelling of sulphur dioxide eruption profiles, Geomatics, Natural Hazards and Risk, 2, 201–216, https://doi.org/10.1080/19475705.2011.590533, 2011.

Sicard, M., Baron, A., Ranaivombola, M., Gantois, D., Millet, T., Sellitto, P., Bègue, N., Bencherif, H., Payen, G., Marquestaut, N., and Duflot, V.: Radiative impact of the Hunga stratospheric volcanic plume: role of aerosols and water vapor over Réunion Island (21° S, 55° E), Atmos. Chem. Phys., 25, 367–381, https://doi.org/10.5194/acp-25-367-2025, 2025.

Skamarock, W. C., Klemp, J. B., Dudhia, J., Gill, D. O., Barker, D. M., Duda, M. G., Huang, X.-Y., Wang, W., and Powers, J. G.: A description of the Advanced Research WRF Version 4, NCAR Technical Note NCAR/TN-556+STR, National Center for Atmospheric Research (NCAR), Boulder, CO, 145 pp., https://doi.org/10.5065/1dfh-6p97, 2019.

Stein, A. F., Draxler, R. R., Rolph, G. D., Stunder, B. J. B., Cohen, M. D., and Ngan, F.: NOAA's HYSPLIT Atmospheric Transport and Dispersion Modeling System, B. Am. Meteorol. Soc., 96, 2059–2077, https://doi.org/10.1175/BAMS-D-14-00110.1, 2015.

Stoffelen, A., Marseille, G. J., Bouttier, F., Vasiljevic, D., De Haan, S., and Cardinali, C.: ADM-Aeolus Doppler wind lidar Observing System Simulation Experiment, Q. J. Roy. Meteor. Soc., 132, 1927–1947, https://doi.org/10.1256/qj.05.83, 2006.

Stoffelen, A., Benedetti, A., Borde, R., Dabas, A., Flamant, P., Forsythe, M., Hardesty, M., Isaksen, L., Källén, E., Körnich, H., Lee, T., Reitebuch, O., Rennie, M., Riishøjgaard, L.-P., Schyberg, H., Straume, A. G., and Vaughan, M.: Wind Profile Satellite Observation Requirements and Capabilities, B. Am. Meteorol. Soc., 101, E2005–E2021, https://doi.org/10.1175/BAMS-D-18-0202.1, 2020.

Stohl, A., Forster, C., Frank, A., Seibert, P., and Wotawa, G.: Technical note: The Lagrangian particle dispersion model FLEXPART version 6.2, Atmos. Chem. Phys., 5, 2461–2474, https://doi.org/10.5194/acp-5-2461-2005, 2005.

Stohl, A., Prata, A. J., Eckhardt, S., Clarisse, L., Durant, A., Henne, S., Kristiansen, N. I., Minikin, A., Schumann, U., Seibert, P., Stebel, K., Thomas, H. E., Thorsteinsson, T., Tørseth, K., and Weinzierl, B.: Determination of time- and height-resolved volcanic ash emissions and their use for quantitative ash dispersion modeling: the 2010 Eyjafjallajökull eruption, Atmos. Chem. Phys., 11, 4333–4351, https://doi.org/10.5194/acp-11-4333-2011, 2011.

Straume-Lindner, A. G., Parrinello, T., Von Bismarck, J., Bley, S., Wernham, D., Kanitz, T., Alvarez, E., Fischey, P., De Laurentis, M., Fehr, T., Ehlers, F., Duc Tran, V., Krisch, I., Reitebuch, O., and Renni, M.: ESA'S Wind Mission Aeolus – Overview, Status and Outlook, in: IGARSS 2021–2021 IEEE International Geoscience and Remote Sensing Symposium, Brussels, Belgium, 11–16 July 2021, 755–758, https://doi.org/10.1109/IGARSS47720.2021.9554007, 2021.

Tackett, J. L., Kar, J., Vaughan, M. A., Getzewich, B. J., Kim, M.-H., Vernier, J.-P., Omar, A. H., Magill, B. E., Pitts, M. C., and Winker, D. M.: The CALIPSO version 4.5 stratospheric aerosol subtyping algorithm, Atmos. Meas. Tech., 16, 745–768, https://doi.org/10.5194/amt-16-745-2023, 2023.

Thompson, G., Field, P. R., Rasmussen, R. M., and Hall, W. D.: Explicit Forecasts of Winter Precipitation Using an Improved Bulk Microphysics Scheme. Part II: Implementation of a New Snow Parameterization, Mon. Weather Rev., 136, 5095–5115, https://doi.org/10.1175/2008MWR2387.1, 2008.

UCAR: Weather Research & Forecasting Model (WRF), UCAR [code], https://doi.org/10.5065/D6MK6B4K, 2025.

Wagner, J., Ansmann, A., Wandinger, U., Seifert, P., Schwarz, A., Tesche, M., Chaikovsky, A., and Dubovik, O.: Evaluation of the Lidar/Radiometer Inversion Code (LIRIC) to determine microphysical properties of volcanic and desert dust, Atmos. Meas. Tech., 6, 1707–1724, https://doi.org/10.5194/amt-6-1707-2013, 2013.

Weitkamp, C. (Ed.): Lidar: range-resolved optical remote sensing of the atmosphere, Springer, New York, NY, 455 pp., ISBN 978-3-540-20227-9, 2005.

Wiegner, M., Gasteiger, J., Groß, S., Schnell, F., Freudenthaler, V., and Forkel, R.: Characterization of the Eyjafjallajökull ash-plume: Potential of lidar remote sensing, Phys. Chem. Earth Pts. A/B/C, 45–46, 79–86, https://doi.org/10.1016/j.pce.2011.01.006, 2012.

WMO: State of the Global Climate 2023, World Meteorological Organization, Geneva, WMO-No. 1347, ISBN 978-92-63-11347-4, https://library.wmo.int/viewer/68835/ (last access: 3 July 2025), 2024.

Zhang, C., Wang, Y., and Hamilton, K.: Improved Representation of Boundary Layer Clouds over the Southeast Pacific in ARW-WRF Using a Modified Tiedtke Cumulus Parameterization Scheme, Mon. Weather Rev., 139, 3489–3513, https://doi.org/10.1175/MWR-D-10-05091.1, 2011.